R. & M. No. 3810

R. & M. No. 3810

PROCUREMENT EXECUTIVE, MINISTRY OF DEFENCE

AERONAUTICAL RESEARCH COUNCIL

REPORTS AND MEMORANDA

A Parametric Computation of Flows and Performance of Rotating Radial Diffusers

By A. K. MAJUMDAR and D. BRIAN SPALDING

Imperial College of Science and Technology

LONDON: HER MAJESTY'S STATIONERY OFFICE

1978

£5 net

A Parametric Computation of Flows and Performance of Rotating Radial Diffusers

By A. K. MAJUMDAR and D. BRIAN SPALDING

Imperial College of Science and Technology

Reports and Memoranda No. 3810*

February, 1977

Summary

A finite-difference procedure is employed to predict the three-dimensional turbulent flow in a rotating radial impeller. The flows are treated as 'partially parabolic' and the turbulence phenomena are represented by a two-equation turbulence model involving the solution of two differential equations, one for the kinetic energy of turbulence and the other for its dissipation rate. Parametric computations have been performed to study:

(a) the effect of rotation on the three-dimensional flow pattern;

(b) the effect of geometrical and flow parameters on the performance of the impeller.

* Replaces A.R.C. 37 188.

LIST OF CONTENTS

1. Introduction

1.1. The Problem Considered

The present paper describes the application of a 'partially-parabolic' procedure to the prediction of three-dimensional turbulent flows in, and the performance parameters of, a radial impeller.

1.2. Past Work

The literature on flow in rotating passages is extensive and has been systematically reviewed by Johnston (1970)[3]. However, few experimental investigations (e.g. Moore (1973)[6], Rothe and Johnston (1975)[10]) on rotating radial impellers have been reported so far. Recently Eckardt (1976)[1] presented a detailed measurement of flow in a 'mixed' flow impeller.

The earlier theoretical investigations on rotating passages are mostly based on the inviscid-flow theory of Stanitz and Ellis (1949)[11]. Recently Moore (1973)[6] presented an analysis, based on an integral method, to predict the secondary flows in a rotating radial impeller. An earlier communication (Pratap *et al.* (1976)[9]) demonstrated that the three-dimensional *parabolic* solution procedure of Patankar and Spalding (1972)[7] was accurate enough only for the situations when the rotational effects are small, and the exit influences are not appreciable. On the other hand, a recent communication (Majumdar and Spalding, 1976)[5] demonstrates that the *partially-parabolic* procedure of Pratap and Spalding (1976)[9] gives a satisfactory agreement with the experimental results of Wagner and Velkoff (1972)[12].

1.3. Present Work

Computations have been performed for the situation illustrated in Fig. 1 by the partially-parabolic procedure. Turbulence is represented by a version of the two-equation turbulence model (Launder and Spalding, 1974)[4] originally proposed by Harlow and Nakayama (1967)[2].

The main objective of the present work is to study the influence of rotation and exit conditions on the three-dimensional flow pattern and to predict the performance parameters (e.g. non-dimensional pressure rise) for various flow and geometrical parameters.

The effects of the following parameters on the non-dimensional pressure-rise characteristics have been studied:

A. Reynolds number ($R \equiv \rho \bar{w}_1 H_1/\mu$)*.
B. Exit-to-inlet radius ratio (r_{tip}/r_{inlet}).
C. Inlet aspect ratio (H_1/B_1).
C. Number of blades ($N \equiv 2\pi/\theta_{IN}$).
E. Exit-to-inlet height ratio (H_2/H_1).

2. Prediction Procedure

2.1. Equations of Motion

With reference to the co-ordinate system shown in Fig. 1, the equations of motion to be solved are:

Continuity:

$$\frac{1}{r}\frac{\partial}{\partial r}(\rho r w)+\frac{1}{r}\frac{\partial}{\partial \theta}(\rho u)+\frac{\partial}{\partial y}(\rho v)=0 \tag{1}$$

Momentum:

r-direction

$$\frac{1}{r}\frac{\partial}{\partial r}(\rho r w^2)+\frac{1}{r}\frac{\partial}{\partial \theta}(\rho u w)+\frac{\partial}{\partial y}(\rho v w)$$
$$=\frac{1}{r^2}\frac{\partial}{\partial \theta}\left(\mu_{eff}\frac{\partial w}{\partial \theta}\right)+\frac{\partial}{\partial y}\left(\mu_{eff}\frac{\partial w}{\partial y}\right)-\frac{\partial p}{\partial r}+\rho\Omega^2 r+2\rho\Omega u+\frac{u^2}{r}-\frac{2\mu_{eff}w}{r^2} \tag{2}$$

---

* The notation is explained in the List of Symbols.

θ-direction

$$\frac{1}{r}\frac{\partial}{\partial r}(\rho rwu)+\frac{1}{r}\frac{\partial}{\partial \theta}(\rho u^2)+\frac{\partial}{\partial y}(\rho uv)$$
$$=\frac{1}{r^2}\frac{\partial}{\partial \theta}\left(\mu_{\text{eff}}\frac{\partial u}{\partial \theta}\right)+\frac{\partial}{\partial y}\left(\mu_{\text{eff}}\frac{\partial u}{\partial y}\right)-\frac{1}{r}\frac{\partial p}{\partial \theta}-2\rho\Omega w-\frac{2\rho uw}{r}+\frac{1}{r^2}\frac{\partial}{\partial \theta}\left(\mu_{\text{eff}}\frac{\partial u}{\partial \theta}\right)$$
$$+\frac{\partial}{\partial y}\left(\frac{\mu_{\text{eff}}}{r}\frac{\partial v}{\partial \theta}\right)+\frac{2}{r}\frac{\partial}{\partial \theta}\left(\frac{\mu_{\text{eff}}w}{r}\right) \tag{3}$$

y-direction

$$\frac{1}{r}\frac{\partial}{\partial r}(\rho rwv)+\frac{1}{r}\frac{\partial}{\partial \theta}(\rho uv)+\frac{\partial}{\partial y}(\rho v^2)$$
$$=\frac{1}{r^2}\frac{\partial}{\partial \theta}\left(\mu_{\text{eff}}\frac{\partial v}{\partial \theta}\right)+\frac{\partial}{\partial y}\left(\mu_{\text{eff}}\frac{\partial v}{\partial y}\right)-\frac{\partial p}{\partial y}+\frac{1}{r}\frac{\partial}{\partial \theta}\left(\mu_{\text{eff}}\frac{\partial u}{\partial y}\right)-\frac{\partial}{\partial y}\left(\mu_{\text{eff}}\frac{\partial v}{\partial y}\right) \tag{4}$$

Here it should be noted that the terms expressing the diffusion of momentum in the radial direction have been omitted, so as to preclude all influences from downstream other than that of pressure.

2.2. Turbulence Model

The effective viscosity, μ_{eff}, appearing in equations (2) to (4) is calculated from a version (Launder and Spalding, 1974[4]) of the two-equation turbulence model first proposed by Harlow and Nakayama (1967)[2]. No special terms have been included for the production and dissipation of turbulence energy by rotational effects.

The governing differential equations for turbulent kinetic energy, k, and its dissipation rate are thus:

Kinetic energy for turbulence:

$$\frac{1}{r}\frac{\partial}{\partial r}(\rho rwk)+\frac{1}{r}\frac{\partial}{\partial \theta}(\rho uk)+\frac{\partial}{\partial y}(\rho vk)$$
$$=\frac{1}{r^2}\frac{\partial}{\partial \theta}\left(\frac{\mu_{\text{eff}}}{\sigma_k}\frac{\partial k}{\partial \theta}\right)+\frac{\partial}{\partial y}\left(\frac{\mu_{\text{eff}}}{\sigma_k}\frac{\partial k}{\partial y}\right)+G-\rho\varepsilon \tag{5}$$

Dissipation rate:

$$\frac{1}{r}\frac{\partial}{\partial r}(\rho rw\varepsilon)+\frac{1}{r}\frac{\partial}{\partial \theta}(\rho u\varepsilon)+\frac{\partial}{\partial y}(\rho v\varepsilon)$$
$$=\frac{1}{r^2}\frac{\partial}{\partial \theta}\left(\frac{\mu_{\text{eff}}}{\sigma_\varepsilon}\frac{\partial \varepsilon}{\partial \theta}\right)+\frac{\partial}{\partial y}\left(\frac{\mu_{\text{eff}}}{\sigma_\varepsilon}\frac{\partial \varepsilon}{\partial y}\right)+\frac{C_1\varepsilon G}{k}-\frac{C_2\rho\varepsilon^2}{k} \tag{6}$$

where

$$G\equiv\mu_t\left[2\left(\frac{\partial v}{\partial y}\right)^2+\frac{2}{r}\frac{\partial v}{\partial \theta}\frac{\partial u}{\partial y}+\left(\frac{\partial w}{\partial y}\right)^2\right.$$
$$\left.+\left(\frac{1}{r}\frac{\partial w}{\partial \theta}\right)^2+\left(\frac{\partial u}{\partial y}\right)^2+2\left(\frac{1}{r}\frac{\partial u}{\partial \theta}+\frac{w}{r}\right)^2\right] \tag{7}$$

The expression for μ_{eff} is:

$$\mu_{\text{eff}}=\mu_l+C_\mu\rho k^2/\varepsilon \tag{8}$$

The model contains five empirical constants, to which are assigned the following regular values (Launder and Spalding, 1974)[4].

C_μ	C_1	C_2	σ_k	σ_ε
0·09	1·44	1·92	1·0	1·3

A 'wall-function' treatment as described by Launder and Spalding (1974)[4] is adopted for the near-wall regions.

2.3. Solution Procedure

The governing differential equations as described in Sections 2.1 and 2.2 are solved by the partially-parabolic procedure of Pratap and Spalding (1976)[9]. The details of the finite-difference equations and the solution procedure appear in Appendix A.

3. Details of Parametric Study

3.1. Flow Situation Considered

Fig. 1 describes the flow situation considered. Plane 1 and Plane 2 indicate the inlet and exit plane respectively.

3.2. Boundary Condition

3.2.1. Inlet Condition. At inlet, the three velocity components (u, v and w) are prescribed.

The radial-velocity distribution has been determined from the inviscid analysis of Moore (1973)[6] which states that:

$$\frac{1}{r}\frac{\partial w}{\partial \theta} = 2\Omega \tag{9}$$

The resulting expression becomes:

$$w(\theta, y) = \bar{w} + 2\Omega r\left(\theta - \frac{\theta_{IN}}{2}\right) \tag{10}$$

where θ_{IN} is the included angle of the diffuser, $\bar{w}$ is the cross-sectional average velocity, Ω is the angular velocity of the diffuser.

Secondary velocities (u and v) are set to zero.

3.2.2. Exit condition. In the majority of the test cases to be described in this report, the pressure distribution in the exit plane conforms to a quasi-one-dimensional inviscid solution (Rothe and Johnston, 1975)[10]. According to this analysis, the pressure distribution at exit plane can be written as

$$\frac{P_{exit} - P_{inlet}}{\frac{1}{2}\rho \bar{w}_1^2} = 1 - \frac{1}{(AR)^2} + 4Ro\left(1 - \frac{\theta}{\theta_{IN}}\right) \tag{11}$$

where

$$P \equiv p - \tfrac{1}{2}\rho\Omega^2 r^2,$$

$$AR \equiv (r_{tip}\theta_{IN})/(r_{inlet}\theta_{IN}),$$

$$Ro \equiv (\Omega r_{inlet}\theta_{IN})/\bar{w}_1 \approx \frac{\Omega B_1}{\bar{w}_1}.$$

One test case has been selected to study the influence of exit-pressure distribution. In that particular test case, the pressure distribution at the exit plane has been assumed to be uniform, i.e. $\partial p/\partial\theta = 0$.

This implies that the fluid at the exit of the duct is discharged into a uniform pressure surroundings.

3.3. Classification of the Test Cases

The present parametric study is constituted of sixty-seven test cases. The parameters considered are already described in Section 1.3. Table 1 describes in detail the scope of the present study.

It may be noted that the test case selected to study the influence of exit pressure distribution has not been classified in Table 1.

3.4. Computational Details

All the test cases (except B1 and B2, see Table 1) have been computed with a 9(θ-direction)×9(y-direction)×21(r-direction) grid nodes. In test cases under serial numbers B1 and B2, the grid nodes in the radial direction are reduced to 16 and 11 respectively as in these test cases the radius ratio has been reduced to 2·0 and 2·5 respectively; the grids in the x- and y-direction are kept the same.

The convergence is checked by examining the magnitude of the normalised integrated mass imbalance, S_m. This is defined as:

$$S_m \equiv \frac{\sum_1^n |\text{mass imbalance in each cell}|}{\text{inlet flow}}$$

where n is the number of cells in a two-directional marching plane.

The maximum permissible value of this non-dimensional measure of mass imbalance was 0·005. Typical computation times was 33 seconds on a CDC 6600 computer for a complete impeller calculation.

4. Results and Discussion

4.1. Effect of Rotation on Flows

In this section, the effects of rotation on overall flow pattern and on the individual flow properties are examined.

4.1.1. Particle tracks. Fig. 2 represents the computer-generated particle tracks at $Ro = 0{\cdot}05$. At inlet, a number of particles are injected near the hub and shroud surfaces, as well as on the centre line.

This demonstrates that the particles in the hub and shroud boundary layers are transported to the suction side. In the central plane, the particles move to the pressure side.

Fig. 3 represents a similar set of particle tracks at $Ro = 0{\cdot}09$. Evidently the flow pattern is similar. However the turning of the tracks is relatively more than that observed in Fig. 2.

A clearer demonstration of the relative turning of the tracks for two different rotation numbers ($Ro = 0{\cdot}05$ and 0·09) has been provided in Figs. 4 and 5.

A detailed discussion of the flow pattern in a rotating rectangular passage has been presented by Majumdar and Spalding (1976)[5]. The same arguments are also applicable here.

4.1.2. Radial velocity distribution, w. Figs. 6 and 7 represent the radial velocity ($\bar{w} = w/\bar{w}_1$) contours at three different radial planes ($r/r_{tip} = 0{\cdot}33$, 0·66 and 0·97) for $Ro = 0{\cdot}05$ and 0·09 respectively.

It should be noted here that, at inlet, the prescribed velocity distribution (equation (10)) has its peak on the suction side. It is observed that, as the flow develops, the velocity maximum is shifted towards the pressure side. When the rotational effects are large (Fig. 7) the retardation of suction-side boundary layer is relatively greater.

4.1.3. 'Blade-to-blade' velocity distribution, u. Figs. 8 and 9 represent the 'blade-to-blade' velocity contours ($\bar{u} = u/\bar{w}$) at three different radial planes ($r/r_{tip} = 0{\cdot}33$, 0·66 and 0·97) for $Ro = 0{\cdot}05$ and 0·09 respectively.

It has been observed that the non-dimensional 'blade-to-blade' component of velocity increases as the flow develops in the radial direction. With the increase of rotational effect, $\bar{u}$ has also been found to increase.

4.1.4. Pressure distribution. Figs. 10 and 11 represent the pressure contours at the central plane ($y/H = 0{\cdot}5$) for $Ro = 0{\cdot}05$ and 0·09 respectively.

These indicate that the predicted pressure distribution in the θ-direction (pressure to suction) is almost linear. It should also be noted that the non-dimensional pressure increases with increase of rotational number.

4.1.5. Turbulence quantities. Figs. 12 and 13 represent the turbulence energy contours at three different radial planes ($r/r_{tip} = 0{\cdot}5$, $0{\cdot}66$ and $0{\cdot}97$) for $Ro = 0{\cdot}05$ and $0{\cdot}09$ respectively.

Turbulence energy has been found to increase with rotational number and, as expected, the turbulence energy is relatively higher near the wall than that in the middle of the duct.

4.1.6. Turbulence length scale. Figs. 14 and 15 represent the turbulence-length-scale contours at three different radial planes ($r/r_{tip} = 0{\cdot}5$, $0{\cdot}66$ and $0{\cdot}97$) for $Ro = 0{\cdot}05$ and $0{\cdot}09$ respectively.

It may be noted that, unlike other quantities, the length-scale distribution is not appreciably affected by the increase of rotational number.

4.2. Effect of Exit Pressure Distribution

Fig. 16 represents the pressure distribution for the test case in which a uniform exit-pressure distribution is assumed. It is observed that, near the exit, the pressures at suction and pressure side adjust themselves to match the uniform exit distribution. This produces a favourable pressure gradient on the pressure side and an adverse gradient on the suction side.

Fig. 17 represents the particle tracks for this test case. It may be noted that the effect of exit conditions is insignificant at inlet, and for the first three quarters of the passage length. The distinctive features of the observed flow pattern from those of test cases examined earlier (Figs. 2 and 3) appear in the last quarter of the passage length. The fluid particles in the hub and shroud boundary layer also move towards the pressure side. This is due to the fact that the flow is accelerated on the pressure side under the action of favourable pressure gradient whereas in the suction side it is decelerated due to adverse pressure gradient. Thus, a relatively larger amount of fluid is discharged from the pressure side.

4.3. Performance of Rotating Impeller

This Section presents the results of parametric studies on the predicted non-dimensional pressure-rise characteristics. The details of the parameters studied have already been described in Section 3.

The predicted results have been compared with the quasi-one-dimensional potential-flow analysis of Rothe and Johnston (1975)[10] (described in Appendix B).

4.3.1. Effect of Reynolds number. The variation of average pressure rise ($C_{p,av}$) with rotation number (Ro) has been shown in Fig. 18. The inviscid solution also appears in the figure.

The difference between the inviscid solution and the predicted solution is evidently due to viscous and secondary losses. It should be noted that the pressure rise increases with the increase of Reynolds number as viscous losses are less at higher Reynolds number.

Tables A1, A2 and A3 provide the tabulated results of the predicted non-dimensional pressure rise and the maximum secondary velocities at exit.

4.3.2. Effect of radius ratio, r_{tip}/r_{inlet}. Fig. 19 represents the variation of non-dimensional pressure rise ($C_{p,av}$) with rotation number (Ro) for different radius ratios. Tables B1, B2 and A2 provide the tabulated result for this study item.

Evidently, with the increase of radius ratio, the pressure rise increases. The predicted distributions are in agreement with the expectation.

4.3.3. Effect of inlet aspect ratio, H_1/B_1. A similar representation of pressure-rise ($C_{p,av}$)~rotation-number (Ro) characteristics for three different inlet aspect ratios have been provided in Fig. 20. Tables C1, C2 and A3 provide the tabulated results for these cases.

It has been found that the pressure rise increases with the increase of inlet aspect ratio.

This is due to the fact that the secondary losses are reduced in a narrower channel. Tabulated results (Table C1, C2 and A3) indicate that the maximum secondary velocities are reduced with an increase of aspect ratio in an otherwise identical situation.

4.3.4. Effect of number of blades ($N \equiv 2\pi/\theta_{IN}$). The effect of the number of blades on $C_{p,av} - Ro$ characteristics has been shown in Fig. 21. Tables D1, D2 and A3 provide the tabulated results for these cases.

It is observed that the pressure rise appreciably increases at higher rotation numbers with an increase of the number of blades.

The cause of such a phenomenon can be explained by examining the magnitude of secondary velocities. It has been found (Tables D1, D2 and A3) that the magnitudes of the secondary velocities are appreciably

reduced by increasing the number of blades. This is due to the fact that the aspect ratio (H/B) increases with the increase of number of blades although the inlet aspect ratio (H_1/B_1) has been kept constant.

4.3.5. Effect of exit to inlet height, H_2/H_1. The effect of exit-to-inlet height ratio on $C_{p,av} \sim Ro$ characteristics has been investigated and appear in Fig. 22. Tables E1, E2 and A3 provide the tabulated results for this study item. The pressure rise is found to decrease with the decrease of exit to inlet height ratio (H_2/H_1).

This observation is also in agreement with the expectation as a decrease of H_2/H_1 implies a reduction of area ratio and hence a decrease of pressure rise.

5. Conclusions

Predictions have been obtained for detailed flow patterns, as well as performance parameters, in radial impellers. The predictions show physical realism and are in reasonable agreement with the expectation. Further tasks are the following:

(1) Extension of the present procedure to handle the curvature effects at inlet.

(2) Predictions of flows in Eckardt's (1976) impeller.

Acknowledgements

This work forms a part of the research sponsored by the Science Research Council, under Grant Number B/RG/6848/7. The computer program was loaned by Combustion, Heat and Momentum Limited. The particle-tracking and contour-plotting programs have been developed by Dr. G. D. Mallinson, whose valuable help the authors wish to acknowledge. Thanks are due to Christine MacKenzie for preparation of the typescript.

LIST OF SYMBOLS

$B = r\theta_{IN}$	Width of the duct.
$C_P = \frac{P_2 - P_{1,\text{suction}}}{\frac{1}{2}\rho \bar{w}_1^2}$	Average pressure recovery.
C_1, C_2, C_μ	Constants in turbulence model.
H	Height of the duct.
k	Kinetic energy of turbulence.
l	Length scale of turbulence.
$P \equiv p - \frac{1}{2}\rho\Omega^2 r^2$	'Reduced pressure'.
p	Static pressure.
r	Distance from the axis of rotation.
$R = \frac{\rho \bar{w}_1 H_1}{\mu_l}$	Reynolds number.
$Ro = \frac{\Omega B_1}{\bar{w}_1}$	Rotation number.
u, v	Secondary velocity components.
w	Longitudinal velocity component.
$\bar{w}$	Cross-sectional average velocity.
y	Cross-stream co-ordinate.
ε	Dissipation rate of turbulence energy.
μ	Kinetic viscosity of fluid.
$\sigma_k, \sigma_\varepsilon$	Prandtl numbers for kinetic energy of turbulence and dissipation rate respectively.
ρ	Density of fluid.
Ω	Angular velocity of the duct.
θ	Cross-stream co-ordinate.

Subscripts

eff	Effective.
l	Laminar.
max	Maximum.
t	Turbulent.
av	Average.
1	Inlet.
2	Exit.
P	Pressure side.
S	Suction side.

REFERENCES

No.	*Author(s)*	*Title, etc*
1	D. Eckardt	Detailed flow investigations within a high speed centrifugal impeller. *J. Fluids Engg.,* Trans. ASME, Vol. 98, Series I, No. 3, pp. 390–402 (1976).
2	F. H. Harlow and P. I. Nakayama ..	Turbulent transport equations. *Physics of Fluids,* Vol. 10, No. 11, pp. 2323–2332 (1967).
3	J. P. Johnston	The effects of rotation on boundary layers in turbo-machine rotors. Rep. MD-24, Thermosciences Div., Dept. of Mech. Engg., Stanford University (1970).
4	B. E. Launder and D. B. Spalding ..	The numerical computations of turbulent flows. *Computer Methods in Applied Mechanics & Engg.,* Vol. 3, pp. 269–289 (1974).
5	A. K. Majumdar and D. B. Spalding	A numerical investigation of three-dimensional flows in a rotating duct by a partially-parabolic procedure. Imperial College, London, Mech. Engg. Dept. Report No. HTS/76/26 (1976).
6	J. Moore	A wake and an eddy in a rotating radial-flow passage. Part 1: Experimental Observations; Part 2: Flow Model. *J. Engg. for Power,* Trans. ASME, Ser. A, Vol. 95, No. 3, pp. 205–219 (1973).
7	S. V. Patankar and D. B. Spalding .	A calculation procedure for heat, mass and momentum transfer in three-dimensional parabolic flows. *Int. J. Heat Mass Transfer,* Vol. 15, pp. 1787–1806 (1972).
8	V. S. Pratap, A. K. Majumdar and D. B. Spalding	Numerical computation of flow in rotating ducts. ASME Paper No. 76-FE-25, 1976.
9	V. S. Pratap and D. B. Spalding ...	A calculation procedure for partially-parabolic flow situations. Imperial College, London, Mech. Engg. Dept. Report No. HTS/75/19 (1975).
10	P. H. Rothe and J. P. Johnston	The effects of system rotation on separation, re-attachment and performance in two-dimensional diffuser. Report PD-17, Thermosciences Div., Dept. of Mech. Engg., Stanford University (1975).
11	J. P. Stanitz and G. O. Ellis	Two-dimensional compressible flow in centrifugal compressors with straight blades. NACA TN 1932, 1949.
12	R. E. Wagner and H. R. Velkoff ...	Measurement of secondary flows in a rotating duct. *J. Engg. for Power,* Trans. ASME, Ser. A, Vol. 94, pp. 261–270.

APPENDIX A

Details of the Partially-Parabolic Solution Procedure

A.1. Finite-Difference Equations

The finite-difference equations are obtained by integrating the differential equations expressing the conservation of mass (equation (1)), momentum (equations (2)–(4)) and the scalar flow properties (equations (5) and (6)) over a control volume. The details of derivation of the finite-difference equations from the differential equations are identical to that in the parabolic calculation procedure and are described by Patankar and Spalding (1972)[7].

The three velocity components and pressures are stored in staggered positions on the finite-difference grid. The definitions of control volumes and storage of variables are shown in Fig. 23.

The difference equations can be stated as follows:

Continuity:

$$C^u[(\rho u)_e-(\rho u)_p]+C^v[(\rho v)_n-(\rho v)_p]+C^w[(\rho w)_p-(\rho w)_u]=0 \tag{A.1}$$

Momenta:

$$U_P=A_N^uU_N+A_S^uU_S+A_E^uU_E+A_W^uU_W+B^u+D^u(p_P-p_W), \tag{A.2}$$

$$V_P=A_N^vV_N+A_S^vV_S+A_E^vV_E+A_W^vV_W+B^v+D^v(p_P-p_S), \tag{A.3}$$

$$W_P=A_N^wW_N+A_S^wW_S+A_E^wW_E+A_W^wW_W+B^w+D^w(p_D-p_P), \tag{A.4}$$

Scalar property, ϕ:

$$\phi_P=A_N^\phi\phi_N+A_S^\phi\phi_S+A_E^\phi\phi_E+A_W^\phi\phi_W+B^\phi \tag{A.5}$$

In the above equations, the A coefficients express the combined effects of convection and diffusion, linking the property at P with its neighbours in the cross-stream plane (Fig. 23); the B coefficients express the contribution of upstream convection and of source terms. The 'C's represent areas of cell faces across which mass is convected, and the 'D's are coefficients linking pressure differences to corresponding velocities. The subscripts P, N, S, E, W, D and U refer to variables at the grid nodes; and the subscripts p, n, s, e, and w denote the variables at the interface locations shown in Fig. 23. The symbol, ϕ, stands for the kinetic energy of turbulence, k and its dissipation rate, ε.

A.2. The Solution Procedure

Main Features

The aim of the solution procedure is to seek a simultaneous solution of the finite-difference equations expressed by equations (A1–A.5). The unknown in these equations are the three velocity components, u, v and w, the pressure, p, and the turbulence properties (k and ε). Since the three momentum equations (A.2, A.3 and A.4) are coupled through the unknown pressure field, it has been necessary to employ an iterative 'space-marching' procedure for their solution. The main features of the present solution procedure are as follows:

(1) The solution procedure employs a guess-and-correct procedure for the calculation of the correct pressure field. Several 'marching' integrations along the predominant flow direction are made through the flow domain and the pressure field is corrected each time so as to bring the velocities into conformity with the continuity equation.

(2) The pressure field is stored as a three-dimensional array and is 'updated' in each 'march' through the flow domain. All other variables and the coefficients are stored as two-dimensional arrays.

(3) The finite-difference equations are solved by a tridiagonal matrix algorithm (TDMA), along lines in the θ and y directions; in this, when the equations are solved along lines of constant-θ, the values of the variables at adjacent y-locations are kept fixed; and vice versa.

Sequence of Calculation Steps

The sequence of calculation steps is the following:

1. The three-dimensional pressure field is first assigned guessed values.

2. A marching integration in the radial (r) direction through the flow domain is initiated; and, from the inlet distributions of u, v and w their distributions at the next downstream plane are calculated. The pressure gradient terms are evaluated from the guessed pressure field; and the coefficients A, B etc. (appearing in equations A.1 to A.5) are evaluated from variables in store at that instant. The equations are solved using a tri-diagonal matrix algorithm (TDMA) (details are given by Patankar and Spalding (1972)[7]).

3. The newly calculated distributions of u, v and w are checked to satisfy the mass continuity at all the control volumes in the current cross-stream plane. The pressure and velocity fields are then corrected by solving a pressure-correction equation so as to remove errors in the mass-continuity. The derivation and the solution of the pressure-correction equation have been described by Pratap and Spalding (1976)[9].

4. The equations for k and ε are solved using the TDMA so as to provide new distributions of effective viscosity, μ_{eff}, appropriate to the new downstream radial plane.

5. Another new downstream radial plane is chosen and the momentum, continuity, k and ε equations are solved as described above. This stepwise march is continued until the end of flow domain is reached. By the end of one complete marching integration, a new three-dimensional distribution of pressure has been obtained.

6. Steps 2, 3, 4 and 5 are then repeated until the continuity error, S_m as defined in section 3.4, have become smaller than a preassigned value (0·005).

APPENDIX B

Inviscid Analysis

In this Section, a simplified inviscid analysis is outlined; this analysis provides an expression for the exit pressure distribution which has been used in the present study.

With the assumption that longitudinal velocity, w, is a function only of longitudinal coordinate, r, the equation for the continuity and momentum for incompressible, potential flow can be written in the following simplified form.

Continuity:

$$\bar{w}(r) r \theta_{\text{IN}} = \bar{w}_1 r_{\text{inlet}} \theta_{\text{IN}} \tag{B.1}$$

θ-momentum:

$$2\Omega \bar{w}(r) = -\frac{1}{\rho r}\frac{\partial P}{\partial \theta} \tag{B.2}$$

r-momentum:

$$\frac{\partial}{\partial r}\left(\frac{w(r)^2}{2}\right) = -\frac{1}{\rho}\frac{\partial p}{\partial r} \tag{B.3}$$

The two-dimensional pressure field, $P(\theta, r)$ can be determined by integrating the momentum equations (Equations B.2 and B.3) with the aid of continuity equation (equation B.1). The resulting exit pressure distribution can then be written as:

$$\frac{P_{\text{exit}} - P_{\text{inlet}} S}{\frac{1}{2}\rho \bar{w}_1^2} = 1 - \left(\frac{r_{\text{inlet}}}{r_{\text{tip}}}\right)^2 + \left(\frac{4\Omega r_{\text{inlet}} \theta_{\text{IN}}}{\bar{w}_1}\right)\left(1 - \frac{\theta}{\theta_{\text{IN}}}\right) \tag{B.4}$$

TABLE 1

Details of Parametric Study

Study items	Serial number*	Flow and geometrical parameters					Remarks†
		Reynolds number R	Radius ratio r_{tip}/r_{inlet}	Inlet aspect ratio H_1/B_1	Number of blades N	Exit to inlet height ratio H_2/H_1	
A. Effect of Reynolds number	A1	$0{\cdot}5\times10^5$	3·00	0·5	24	1	Table A.1
	A2	1×10^5	3·00	0·5	24	1	Table A.2
	A3	2×10^5	3·00	0·5	24	1	Table A.3
B. Effect of radius ratio	B1	1×10^5	2·0	0·5	24	1	Table B.1
	B2	1×10^5	2·5	0·5	24	1	Table B.2
	B3	1×10^5	3·0	0·5	24	1	Table A.2
C. Effect of inlet aspect ratio	C1	2×10^5	3·0	1·5	24	1	Table C.1
	C2	2×10^5	3·0	1·0	24	1	Table C.2
	C3	2×10^5	3·0	0·5	24	1	Table A.3
D. Effect of number of blades	D1	2×10^5	3·0	0·5	36	1	Table D.1
	D2	2×10^5	3·0	0·5	30	1	Table D.2
	D3	2×10^5	3·0	0·5	24	1	Table A.3
E. Effect of exit to inlet height ratio	E1	2×10^5	3·0	0·5	24	0·64	Table E.1
	E2	2×10^5	3·0	0·5	24	0·80	Table E.2
	E3	2×10^5	3·0	0·5	24	1·00	Table A.3

* Under each serial number computations have been performed for six different rotation numbers ($Ro = 0{\cdot}01, 0{\cdot}03, 0{\cdot}05, 0{\cdot}07, 0{\cdot}09, 0{\cdot}11$).

† Tabulated results for each item appear in the table number shown in this column.

TABLE A.1

Tabulated Results for Item No. A.1

$r_{tip}/r_{inlet} = 3{\cdot}0$

$H_1/B_1 = 0{\cdot}5$

$H_2/H_1 = 1{\cdot}0$

$N = 24$

$R = 0{\cdot}5 \times 10^4$

$$C_{P,P} = \frac{(p_{exit,pressure} - \frac{1}{2}\rho\Omega^2 r_{tip}^2) - (p_{inlet,suction} - \frac{1}{2}\rho\Omega^2 r_{inlet}^2)}{\frac{1}{2}\rho\bar{w}_1^2}$$

$$C_{P,S} = \frac{(p_{exit,suction} - \frac{1}{2}\rho\Omega^2 r_{tip}^2) - (p_{inlet,suction} - \frac{1}{2}\rho\Omega^2 r_{inlet}^2)}{\frac{1}{2}\rho\bar{w}_1^2}$$

$C_{P,av} = \frac{1}{2}(C_{P,P} + C_{P,S})$

Rotation number Ro $\left(\frac{\Omega B_1}{\bar{w}_1}\right)$	Non-dimensional pressure rise						Predicted maximum secondary velocities at exit plane	
	Predictions			Inviscid solution				
	$C_{P,P}$	$C_{P,S}$	$C_{P,av}$	$C_{P,P}$	$C_{P,S}$	$C_{P,av}$	$\bar{u} \equiv \frac{\lvert u_{max}\rvert}{\bar{w}_1}$	$\bar{v} \equiv \frac{\lvert v_{max}\rvert}{\bar{w}_1}$
0·01	0·7442	0·7176	0·7309	0·9269	0·8909	0·9089	0·0132	0·0024
0·03	0·8022	0·7223	0·7623	1·003	0·8949	0·949	0.0372	0·00678
0·05	0·8613	0·7281	0·7947	1·079	0·8989	0·989	0·0576	0·0111
0·07	0·9211	0·7347	0·8279	1·155	0·9029	1·029	0·073	0·0147
0·09	0·9811	0·7414	0·8613	1·231	0·9069	1·069	0·0833	0·0175
0·11	1·041	0·748	0·8945	1·307	0·9109	1·109	0·0898	0·0193

TABLE A.2

Tabulated Results for Item No. A.2.

$r_{tip}/r_{inlet} = 3{\cdot}0$

$H_1/B_1 = 0{\cdot}5$

$H_2/H_1 = 1{\cdot}0$

$N = 24$

$R = 1\times10^5$

$$C_{P,P} = \frac{(p_{exit,pressure} - \frac{1}{2}\rho\Omega^2 r_{tip}^2) - (p_{inlet,suction} - \frac{1}{2}\rho\Omega^2 r_{inlet}^2)}{\frac{1}{2}\rho\bar{w}_1^2}$$

$$C_{P,S} = \frac{(p_{exit,suction} - \frac{1}{2}\rho\Omega^2 r_{tip}^2) - (p_{inlet,suction} - \frac{1}{2}\rho\Omega^2 r_{inlet}^2)}{\frac{1}{2}\rho\bar{w}_1^2}$$

$C_{P,av} = \frac{1}{2}(C_{P,P} + C_{P,S})$

Rotation number Ro $\left(\frac{\Omega B_1}{\bar{w}_1}\right)$	Non-dimensional pressure rise						Predicted maximum Secondary velocities at exit plane	
	Predictions			Inviscid solution				
	$C_{P,P}$	$C_{P,S}$	$C_{P,av}$	$C_{P,P}$	$C_{P,S}$	$C_{P,av}$	$\bar{u} \equiv \frac{\lvert u_{max}\rvert}{\bar{w}_1}$	$\bar{v} \equiv \frac{\lvert v_{max}\rvert}{\bar{w}_1}$
0·01	0·7556	0·729	0·7423	0·9269	0·8909	0·9089	0·0126	0·0022
0·03	0·8135	0·7336	0·7735	1·003	0·8949	0·949	0·0357	0·0063
0·05	0·8727	0·7395	0·8061	1·079	0·8989	0·989	0·0555	0·0103
0·07	0·9326	0·7462	0·8394	1·155	0·9029	1·029	0·0709	0·01377
0·09	0·9931	0·7534	0·8733	1·231	0·9069	1·069	0·0817	0·0165
0·11	1·054	0·7610	0·9075	1·307	0·9109	1·109	0·0915	0·0185

TABLE A.3.

Tabulated Results for Item No. A.3.

$r_{tip}/r_{inlet} = 3{\cdot}0$

$H_1/B_1 = 0{\cdot}5$

$H_2/H_1 = 1{\cdot}0$

$N = 24$

$R = 2\times10^5$

$$C_{P,P} = \frac{(p_{exit,pressure} - \frac{1}{2}\rho\Omega^2 r_{tip}^2) - (p_{inlet,suction} - \frac{1}{2}\rho\Omega^2 r_{inlet}^2)}{\frac{1}{2}\rho\bar{w}_1^2}$$

$$C_{P,S} = \frac{(p_{exit,suction} - \frac{1}{2}\rho\Omega^2 r_{tip}^2) - (p_{inlet,suction} - \frac{1}{2}\rho\Omega^2 r_{inlet}^2)}{\frac{1}{2}\rho\bar{w}_1^2}$$

$C_{P,av} = \frac{1}{2}(C_{P,P} + C_{P,S})$

Rotation number Ro $\left(\frac{\Omega B_1}{\bar{w}_1}\right)$	Non-dimensional pressure rise						Predicted maximum secondary velocities at exit plane	
	Predictions			Inviscid solution				
	$C_{P,P}$	$C_{P,S}$	$C_{P,av}$	$C_{P,P}$	$C_{P,S}$	$C_{P,av}$	$\bar{u} \equiv \frac{\lvert u_{max}\rvert}{\bar{w}_1}$	$\bar{v} \equiv \frac{\lvert v_{max}\rvert}{\bar{w}_1}$
0·01	0·7671	0·7404	0·7538	0·9269	0·8909	0·9089	0·012	0·002
0·03	0·8254	0·7455	0·7854	1·003	0·8949	0·949	0·0342	0·006
0·05	0·8855	0·7524	0·8189	1·079	0·8989	0·989	0·0535	0·009
0·07	0·9474	0·7609	0·8542	1·155	0·9029	1·03	0·0686	0·013
0·09	1·011	0·7714	0·8912	1·231	0·9069	1·07	0·0805	0·0155
0·11	1·077	0·7839	0·9304	1·307	0·9109	1·109	0·0923	0·0176

TABLE B.1.

Tabulated Results for Item No. B.1.

$r_{tip}/r_{inlet} = 2{\cdot}0$

$H_1/B_1 = 0{\cdot}5$

$H_2/H_1 = 1{\cdot}0$

$N = 24$

$R = 1 \times 10^5$

$$C_{P,P} = \frac{(p_{exit,pressure} - \frac{1}{2}\rho\Omega^2 r_{tip}^2) - (p_{inlet,suction} - \frac{1}{2}\rho\Omega^2 r_{inlet}^2)}{\frac{1}{2}\rho\bar{w}_1^2}$$

$$C_{P,S} = \frac{(p_{exit,suction} - \frac{1}{2}\rho\Omega^2 r_{tip}^2) - (p_{inlet,suction} - \frac{1}{2}\rho\Omega^2 r_{inlet}^2)}{\frac{1}{2}\rho\bar{w}_1^2}$$

$$C_{P,av} = \tfrac{1}{2}(C_{P,P} + C_{P,S})$$

Rotation number Ro $\left(\frac{\Omega B_1}{\bar{w}_1}\right)$	Non-dimensional pressure rise						Predicted maximum secondary velocities at exit plane	
	Predictions			Inviscid solution				
	$C_{P,P}$	$C_{P,S}$	$C_{P,av}$	$C_{P,P}$	$C_{P,S}$	$C_{P,av}$	$\bar{u} \equiv \frac{\lvert u_{max}\rvert}{\bar{w}_1}$	$\bar{v} \equiv \frac{\lvert v_{max}\rvert}{\bar{w}_1}$
0·01	0·6633	0·6367	0·65	0·788	0·752	0·77	0·0055	0·0024
0·03	0·7144	0·6345	0·6745	0·8640	0·7560	0·81	0·0137	0·0031
0·05	0·7599	0·6267	0·6933	0·94	0·76	0·85	0·0227	0·0043
0·07	0·7999	0·6135	0·7067	1·016	0·7640	0·89	0·0317	0·0058
0·09	0·8344	0·5947	0·7145	1·092	0·7680	0·93	0·0407	0·0073
0·11	0·8634	0·5704	0·7169	1·168	0·772	0·97	0·0504	0·0087

TABLE B.2.

Tabulated Results for Item No. B.2.

$r_{tip}/r_{inlet} = 2{\cdot}5$

$H_1/B_1 = 0{\cdot}5$

$H_2/H_1 = 1{\cdot}0$

$N = 24$

$R = 1 \times 10^5$

$$C_{P,P} = \frac{(p_{exit,pressure} - \frac{1}{2}\rho\Omega^2 r_{tip}^2) - (p_{inlet,suction} - \frac{1}{2}\rho\Omega^2 r_{inlet}^2)}{\frac{1}{2}\rho\bar{w}_1^2}$$

$$C_{P,S} = \frac{(p_{exit,suction} - \frac{1}{2}\rho\Omega^2 r_{tip}^2) - (p_{inlet,suction} - \frac{1}{2}\rho\Omega^2 r_{inlet}^2)}{\frac{1}{2}\rho\bar{w}_1^2}$$

$C_{P,av} = \frac{1}{2}(C_{P,P} + C_{P,S})$

Rotation number Ro $\left(\frac{\Omega B_1}{\bar{w}_1}\right)$	Non-dimensional pressure rise						Predicted maximum secondary velocities at exit plane	
	Predictions			Inviscid solution				
	$C_{P,P}$	$C_{P,S}$	$C_{P,av}$	$C_{P,P}$	$C_{P,S}$	$C_{P,av}$	$\bar{u} \equiv \frac{\lvert u_{max}\rvert}{\bar{w}_1}$	$\bar{v} \equiv \frac{\lvert v_{max}\rvert}{\bar{w}_1}$
0·01	0·7241	0·6975	0·7108	0·878	0·842	0·86	0·0085	0·0025
0·03	0·778	0·6981	0·7381	0·9540	0·846	0·9	0·0207	0·0042
0·05	0·8292	0·6961	0·7627	1·03	0·85	0·94	0·0351	0·0059
0·07	0·8779	0·6914	0·7847	1·106	0·8540	0·98	0·0505	0·0095
0·09	0·9239	0·6842	0·8040	1·182	0·8580	1·02	0·0620	0·0130
0·11	0·9672	0·6742	0·8207	1·258	0·862	1·06	0·0731	0·0142

TABLE C.1.

Tabulated Results for Item No. C.1.

$r_{tip}/r_{inlet} = 3{\cdot}0$

$H_1/B_1 = 1{\cdot}5$

$H_2/H_1 = 1{\cdot}0$

$N = 24$

$R = 2\times10^5$

$$C_{P,P} = \frac{(p_{exit,pressure} - \frac{1}{2}\rho\Omega^2 r_{tip}^2) - (p_{inlet,suction} - \frac{1}{2}\rho\Omega^2 r_{inlet}^2)}{\frac{1}{2}\rho\bar{w}_1^2}$$

$$C_{P,S} = \frac{(p_{exit,suction} - \frac{1}{2}\rho\Omega^2 r_{tip}^2) - (p_{inlet,suction} - \frac{1}{2}\rho\Omega^2 r_{inlet}^2)}{\frac{1}{2}\rho\bar{w}_1^2}$$

$$C_{P,av} = \tfrac{1}{2}(C_{P,P} + C_{P,S})$$

Rotation number Ro $\left(\frac{\Omega B_1}{\bar{w}_1}\right)$	Non-dimensional pressure rise						Predicted maximum secondary velocities at exit plane	
	Predictions			Inviscid solution				
	$C_{P,P}$	$C_{P,S}$	$C_{P,av}$	$C_{P,P}$	$C_{P,S}$	$C_{P,av}$	$\bar{u} \equiv \frac{\lvert u_{max}\rvert}{\bar{w}_1}$	$\bar{v} \equiv \frac{\lvert v_{max}\rvert}{\bar{w}_1}$
0·01	0·7966	0·7701	0·7834	0·9269	0·8909	0·9089	0·0107	0·003
0·03	0·8539	0·774	0·8139	1·003	0·8949	0·949	0·028	0·007
0·05	0·9123	0·779	0·8457	1·079	0·8989	0·989	0·047	0·011
0.07	0·972	0·785	0·8785	1·155	0·9029	1·029	0·066	0·014
0·09	1·033	0·7933	0·9131	1·231	0·9069	1·069	0·087	0·017

TABLE C.2.

Tabulated Results for Item No. C.2.

$r_{tip}/r_{inlet} = 3{\cdot}0$

$H_1/B_1 = 1{\cdot}0$

$H_2/H_1 = 1{\cdot}0$

$N = 24$

$R = 2\times10^5$

$$C_{P,P} = \frac{(p_{exit,pressure} - \frac{1}{2}\rho\Omega^2 r_{tip}^2) - (p_{inlet,suction} - \frac{1}{2}\rho\Omega^2 r_{inlet}^2)}{\frac{1}{2}\rho\bar{w}_1^2}$$

$$C_{P,S} = \frac{(p_{exit,suction} - \frac{1}{2}\rho\Omega^2 r_{tip}^2) - (p_{inlet,suction} - \frac{1}{2}\rho\Omega^2 r_{inlet}^2)}{\frac{1}{2}\rho\bar{w}_1^2}$$

$$C_{P,av} = \tfrac{1}{2}(C_{P,P} + C_{P,S})$$

Rotation number Ro $\left(\frac{\Omega B_1}{\bar{w}_1}\right)$	Non-dimensional pressure rise						Predicted maximum secondary velocities at exit plane	
	Predictions			Inviscid solution				
	$C_{P,P}$	$C_{P,S}$	$C_{P,av}$	$C_{P,P}$	$C_{P,S}$	$C_{P,av}$	$\bar{u} \equiv \frac{\lvert u_{max}\rvert}{\bar{w}_1}$	$\bar{v} \equiv \frac{\lvert v_{max}\rvert}{\bar{w}_1}$
0·01	0·7897	0·7631	0·7764	0·9269	0·8909	0·9089	0·0115	0·003
0·03	0·8473	0·7674	0·8074	1·003	0·8949	0·949	0·0303	0·008
0·05	0·9061	0·7729	0·8395	1·079	0·8989	0·989	0·049	0·0122
0·07	0·9664	0·7799	0·8732	1·155	0·9029	1·029	0·068	0·0165
0·09	1·028	0·7885	0·9083	1·231	0·9069	1·069	0·0866	0·0195

TABLE D.1.

Tabulated Results for Item No. D.1.

$r_{tip}/r_{inlet} = 3{\cdot}0$

$H_1/B_1 = 0{\cdot}5$

$H_2/H_1 = 1{\cdot}0$

$N = 36$

$R = 2\times10^5$

$$C_{P,P} = \frac{(p_{exit,pressure} - \frac{1}{2}\rho\Omega^2 r_{tip}^2) - (p_{inlet,suction} - \frac{1}{2}\rho\Omega^2 r_{inlet}^2)}{\frac{1}{2}\rho\bar{w}_1^2}$$

$$C_{P,S} = \frac{(p_{exit,suction} - \frac{1}{2}\rho\Omega^2 r_{tip}^2) - (p_{inlet,suction} - \frac{1}{2}\rho\Omega^2 r_{inlet}^2)}{\frac{1}{2}\rho\bar{w}_1^2}$$

$$C_{P,av} = \tfrac{1}{2}(C_{P,P} + C_{P,S})$$

Rotation number Ro $\left(\frac{\Omega B_1}{\bar{w}_1}\right)$	Non-dimensional pressure rise						Predicted maximum secondary velocities at exit plane	
	Predictions			Inviscid solution				
	$C_{P,P}$	$C_{P,S}$	$C_{P,av}$	$C_{P,P}$	$C_{P,S}$	$C_{P,av}$	$\bar{u} \equiv \frac{\lvert u_{max}\rvert}{\bar{w}_1}$	$\bar{v} \equiv \frac{\lvert v_{max}\rvert}{\bar{w}_1}$
0·01	0·7532	0·7266	0·7399	0·9269	0·8909	0·9089	0·0159	0·0029
0·03	0·8163	0·7364	0·7764	1·003	0·8949	0·949	0·0427	0·0091
0·05	0·8865	0·7533	0·8199	1·079	0·8989	0·989	0·0610	0·0142
0·07	0·9664	0·7801	0·8733	1·155	0·9029	1·029	0·0687	0·0164
0·09	1·061	0·8217	0·9414	1·231	0·9069	1·069	0·0665	0·0166
0·11	1·179	0·8863	1·0327	1·307	0·9109	1·109	0·0569	0·0151

TABLE D.2.

Tabulated Results for Item No. D.2.

$r_{tip}/r_{inlet} = 3{\cdot}0$

$H_1/B_1 = 0{\cdot}5$

$H_2/H_1 = 1{\cdot}0$

$N = 30$

$R = 2\times10^5$

$$C_{P,P} = \frac{(p_{exit,pressure} - \frac{1}{2}\rho\Omega^2 r_{tip}^2) - (p_{inlet,suction} - \frac{1}{2}\rho\Omega^2 r_{inlet}^2)}{\frac{1}{2}\rho\bar{w}_1^2}$$

$$C_{P,S} = \frac{(p_{exit,suction} - \frac{1}{2}\rho\Omega^2 r_{tip}^2) - (p_{inlet,suction} - \frac{1}{2}\rho\Omega^2 r_{inlet}^2)}{\frac{1}{2}\rho\bar{w}_1^2}$$

$C_{P,av} = \frac{1}{2}(C_{P,P} + C_{P,S})$

Rotation number Ro $\left(\frac{\Omega B_1}{\bar{w}_1}\right)$	Non-dimensional pressure rise						Predicted maximum secondary velocities at exit plane	
	Predictions			Inviscid solution				
	$C_{P,P}$	$C_{P,S}$	$C_{P,av}$	$C_{P,P}$	$C_{P,S}$	$C_{P,av}$	$\bar{u} \equiv \frac{\lvert u_{max}\rvert}{\bar{w}_1}$	$\bar{v} \equiv \frac{\lvert v_{max}\rvert}{\bar{w}_1}$
0·01	0·7606	0·7339	0·7473	0·9269	0·8909	0·9089	0·0139	0·0026
0·03	0·8208	0·7409	0·7809	1·003	0·8949	0·949	0·0388	0·0077
0·05	0·8847	0·7515	0·8181	1·079	0·8989	0·989	0·0582	0·0124
0·07	0·9528	0·766	0·8594	1·155	0·9029	1·029	0·0705	0·01604
0·09	1·027	0·7868	0·9069	1·231	0·9069	1·069	0·0755	0·01816
0·11	1·108	0·8153	0·9617	1·307	0·9109	1·109	0·075	0·01904

TABLE E.1.

Tabulated Results for Item No. E. 1.

$r_{tip}/r_{inlet} = 3{\cdot}0$

$H_1/B_1 = 0{\cdot}5$

$H_2/H_1 = 0{\cdot}64$

$N = 24$

$R = 2 \times 10^5$

$$C_{P,P} = \frac{(p_{exit,pressure} - \frac{1}{2}\rho\Omega^2 r_{tip}^2) - (p_{inlet,suction} - \frac{1}{2}\rho\Omega^2 r_{inlet}^2)}{\frac{1}{2}\rho\bar{w}_1^2}$$

$$C_{P,S} = \frac{(p_{exit,suction} - \frac{1}{2}\rho\Omega^2 r_{tip}^2) - (p_{inlet,suction} - \frac{1}{2}\rho\Omega^2 r_{inlet}^2)}{\frac{1}{2}\rho\bar{w}_1^2}$$

$C_{P,av} = \frac{1}{2}(C_{P,P} + C_{P,S})$

Rotation number Ro $\left(\frac{\Omega B_1}{\bar{w}_1}\right)$	Non-dimensional pressure rise						Predicted maximum secondary velocities at exit plane	
	Predictions			Inviscid solution				
	$C_{P,P}$	$C_{P,S}$	$C_{P,av}$	$C_{P,P}$	$C_{P,S}$	$C_{P,av}$	$\bar{u} \equiv \frac{\lvert u_{max}\rvert}{\bar{w}_1}$	$\bar{v} \equiv \frac{\lvert v_{max}\rvert}{\bar{w}_1}$
0·01	0·6321	0·6054	0·6188	0·7667	0·7307	0·7487	0·009	0·022
0·03	0·6895	0·6096	0·6495	0·8427	0·7347	0·7887	0·026	0·023
0·05	0·7479	0·6147	0·6813	0·9187	0·7387	0·8287	0·0437	0·0245
0·07	0·8076	0·6212	0·7144	0·9947	0·7427	0·8687	0·0604	0·0257
0·09	0·8692	0·6295	0·7494	1·071	0·7467	0·9089	0·0763	0·027
0·11	0·933	0·6403	0·7867	1·147	0·7507	0·9489	0·0915	0·028

Table E.2.

Tabulated Results for Item No. E.2.

$r_{tip}/r_{inlet} = 3{\cdot}0$

$H_1/B_1 = 0{\cdot}5$

$H_2/H_1 = 0{\cdot}8$

$N = 24$

$R = 2\times10^5$

$$C_{P,P} = \frac{(p_{exit,pressure} - \frac{1}{2}\rho\Omega^2 r_{tip}^2) - (p_{inlet,suction} - \frac{1}{2}\rho\Omega^2 r_{inlet}^2)}{\frac{1}{2}\rho\bar{w}_1^2}$$

$$C_{P,S} = \frac{(p_{exit,suction} - \frac{1}{2}\rho\Omega^2 r_{tip}^2) - (p_{inlet,suction} - \frac{1}{2}\rho\Omega^2 r_{inlet}^2)}{\frac{1}{2}\rho\bar{w}_1^2}$$

$$C_{P,av} = \tfrac{1}{2}(C_{P,P} + C_{P,S})$$

Rotation number $Ro\left(\frac{\Omega B_1}{\bar{w}_1}\right)$	Non-dimensional pressure rise						Predicted maximum secondary velocities at exit plane	
	Predictions			Inviscid solution				
	$C_{P,P}$	$C_{P,S}$	$C_{P,av}$	$C_{P,P}$	$C_{P,S}$	$C_{P,av}$	$\bar{u} \equiv \frac{\lvert u_{max}\rvert}{\bar{w}_1}$	$\bar{v} \equiv \frac{\lvert v_{max}\rvert}{\bar{w}_1}$
0·01	0·7230	0·6963	0·7097	0·8664	0·8284	0·8474	0·0076	0·011
0·03	0·7805	0·7006	0·7406	0·9404	0·8324	0·8864	0·0195	0·0123
0·05	0·8392	0·7060	0·7726	1·016	0·8364	0·9262	0·0306	0·0133
0·07	0·8994	0·7129	0·8062	1·092	0·8404	0·9662	0·0398	0·0156
0·09	0·9615	0·7218	0·8417	1·168	0·8444	1·006	0·0462	0·0151
0·11	1·026	0·733	0·8795	1·244	0·8484	1·046	0·0496	0·0202

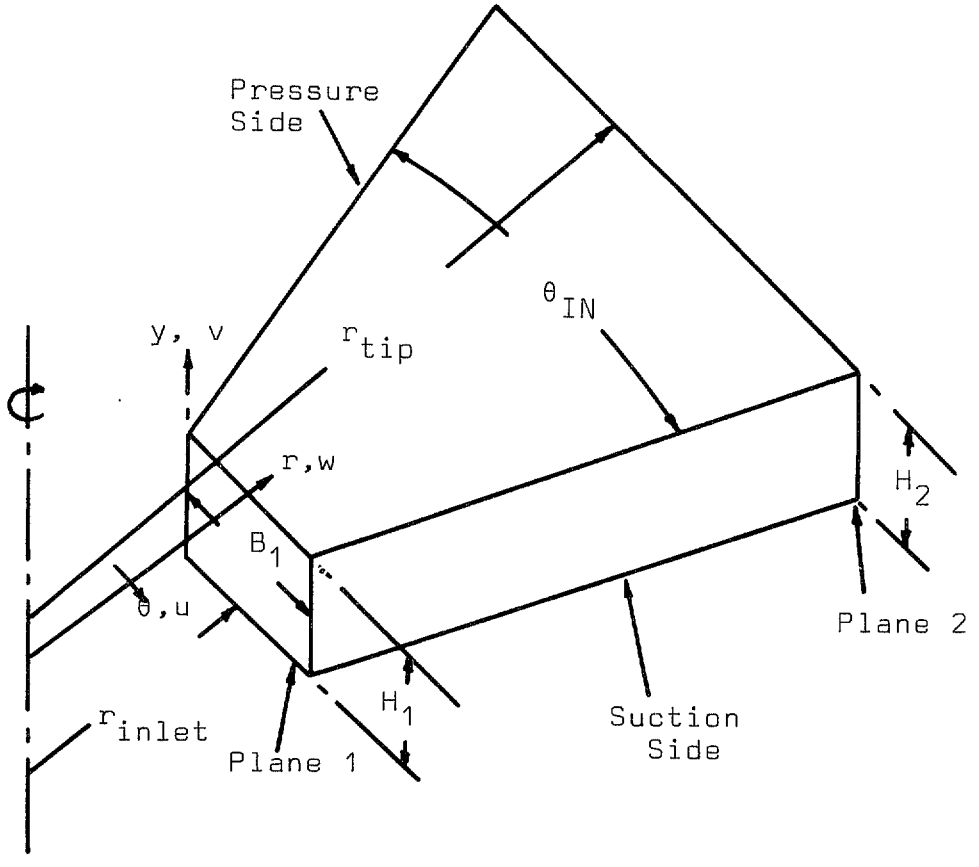

FIG. 1. A schematic view of the rotating diffuser and the co-ordinate system.

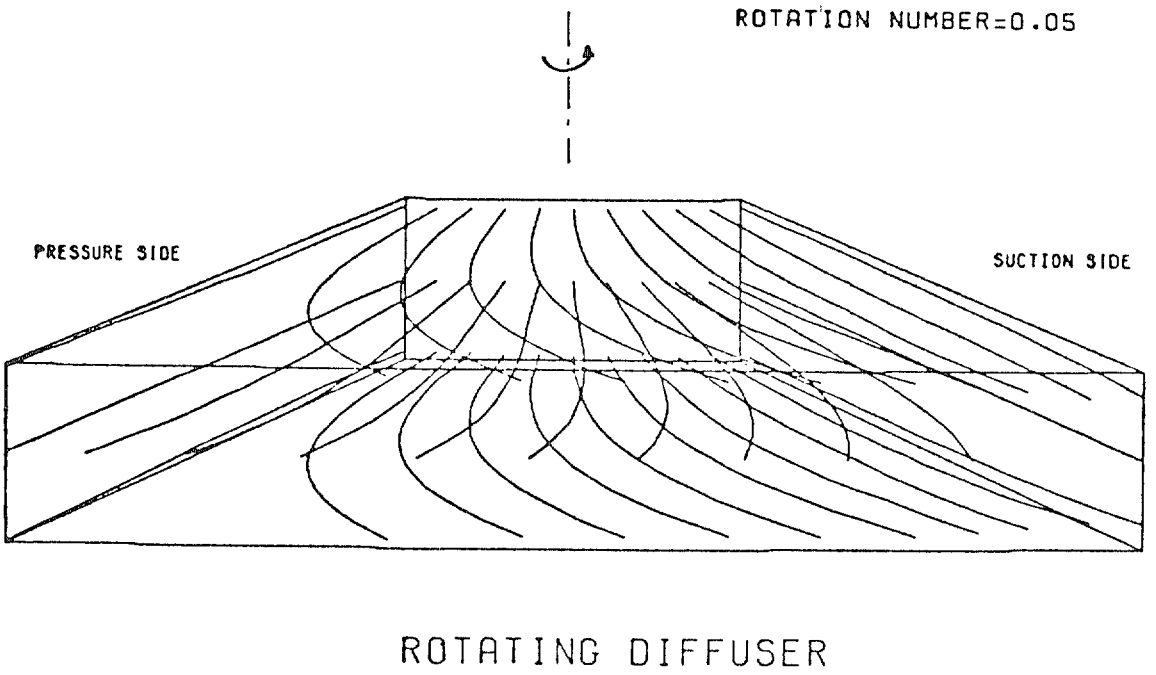

FIG. 2. A perspective view of particle tracks in rotating diffusers; $Ro = 0{\cdot}05$, $R = 2 = 10^5$, $N = 24$, $H_2/H_1 = 1$, $H_1/B_1 = 0{\cdot}5$.

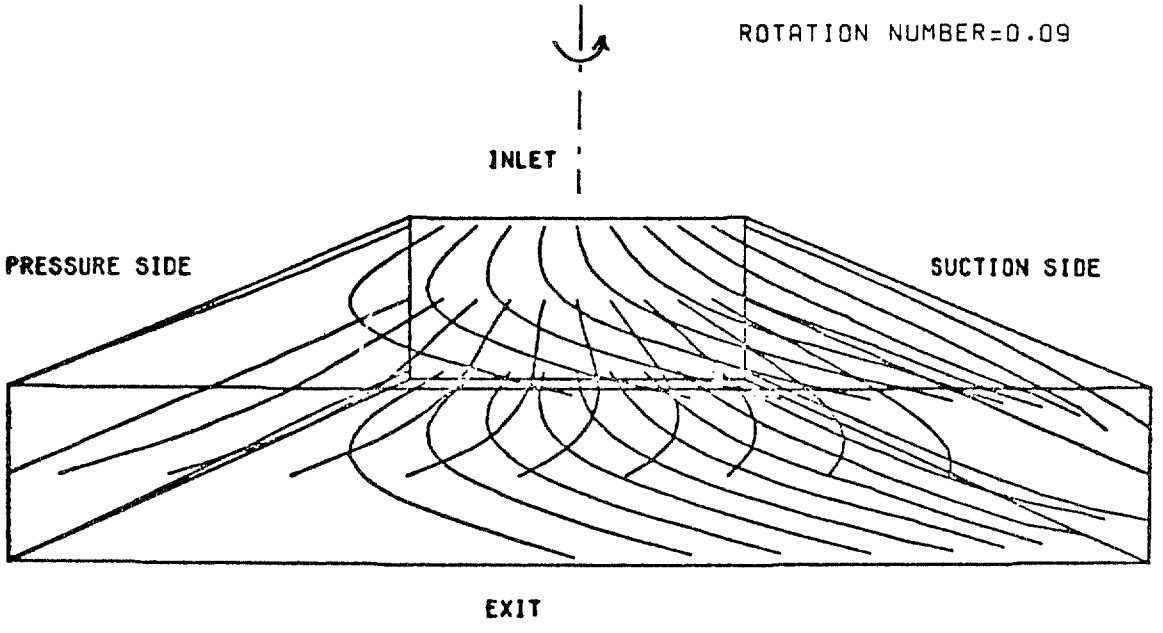

FIG. 3. A perspective view of particle tracks in rotating diffuser; $Ro = 0{\cdot}09$, $R = 2 \times 10^5$, $N = 24$, $H_2/H_1 = 1$, $H_1/B_1 = 0{\cdot}5$.

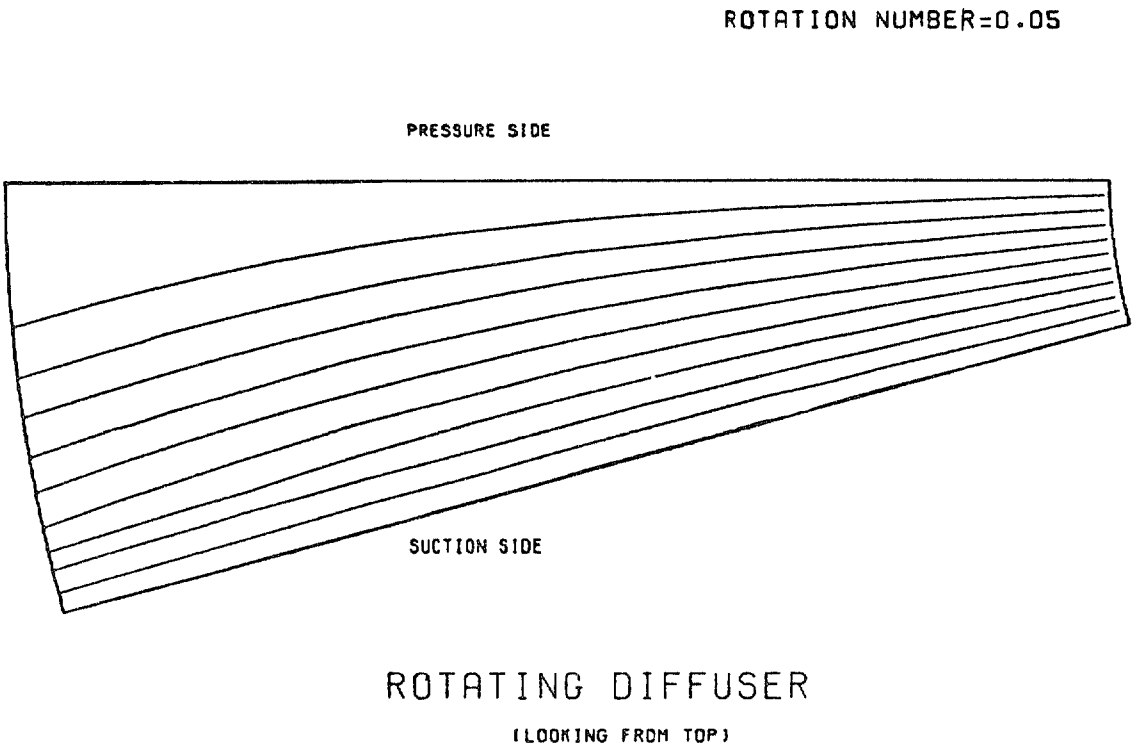

FIG. 4. A plan view of the particle tracks; particles are injected in the inlet plane at the boundary layer near the shroud (top) surface; $Ro = 0{\cdot}05$, $R = 2 \times 10^5$, $N = 24$, $H_2/H_1 = 1$, $H_1/B_1 = 0{\cdot}5$.

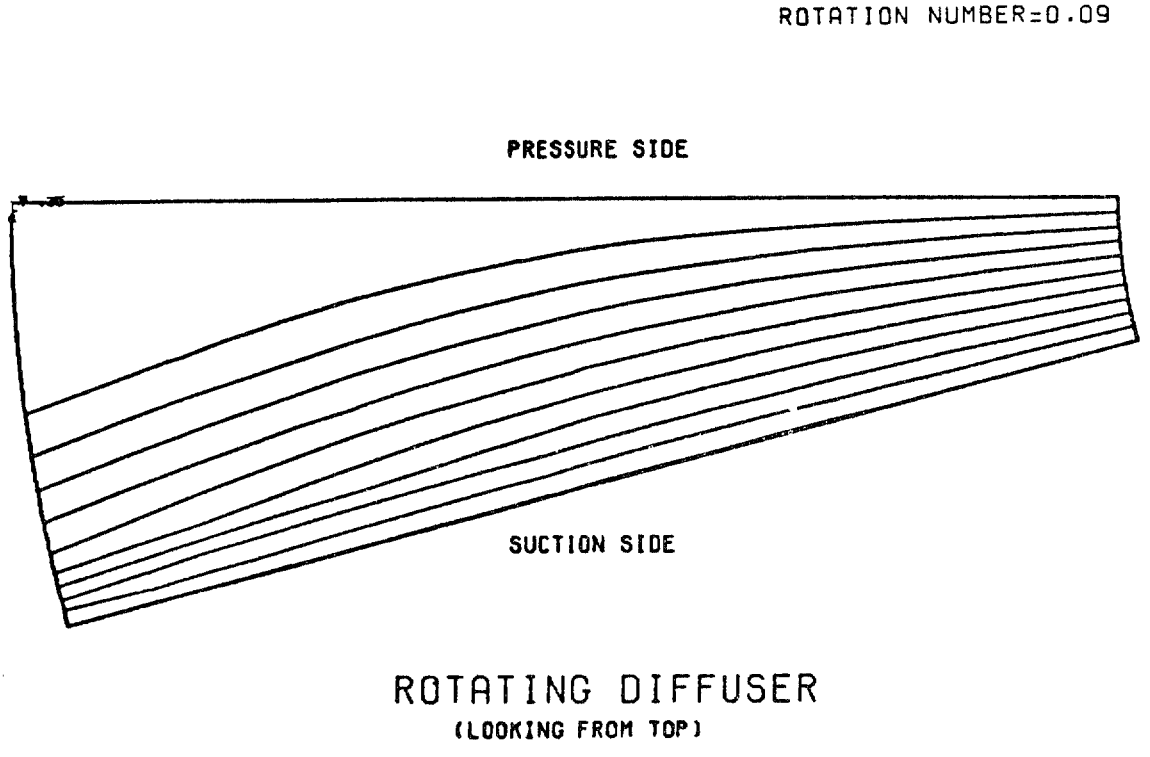

FIG. 5. A plan view of the particle tracks; particles are injected in the inlet plane at the boundary layer near the shroud (top) surface; $Ro = 0{\cdot}09$, $R = 2 \times 10^5$, $N = 24$, $H_2/H_1 = 1$, $H_1/B_1 = 0{\cdot}5$.

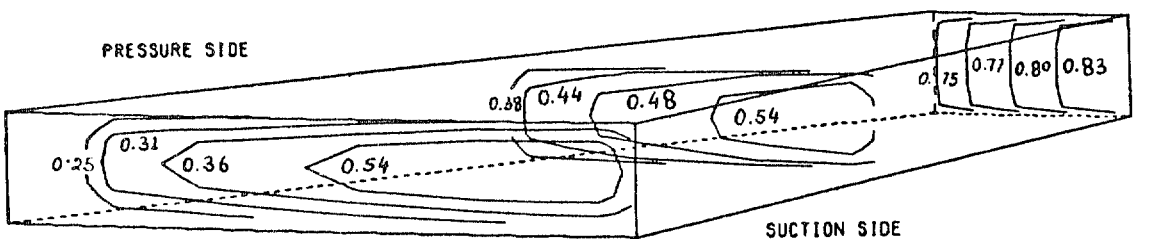

FIG. 6. A perspective view of the radial velocity contours [$\bar{w} = w/\bar{w}$], at three different radial planes ($r/r_{tip} = 0{\cdot}33, 0{\cdot}66, 0{\cdot}97$); $Ro = 0{\cdot}05$, $R = 2 \times 10^5$, $N = 24$, $H_2/H_1 = 1$, $H_1/B_1 = 0{\cdot}5$.

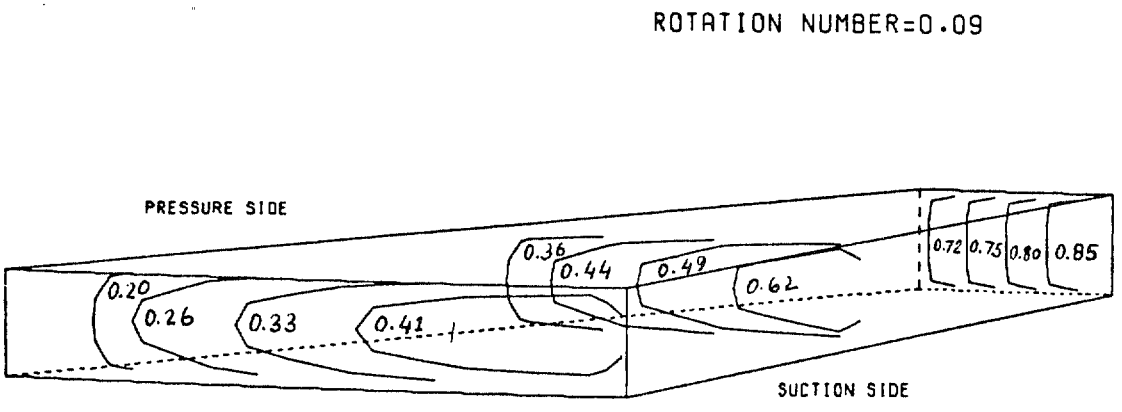

FIG. 7. A perspective view of the radial velocity contours [$\bar{w} = w/w_1$] at three different radial planes ($r/r_{tip} = 0{\cdot}33, 0{\cdot}66, 0{\cdot}97$); $Ro = 0{\cdot}09$, $R = 2 \times 10^5$, $N = 24$, $H_2/H_1 = 1$, $H_1/B_1 = 0{\cdot}5$.

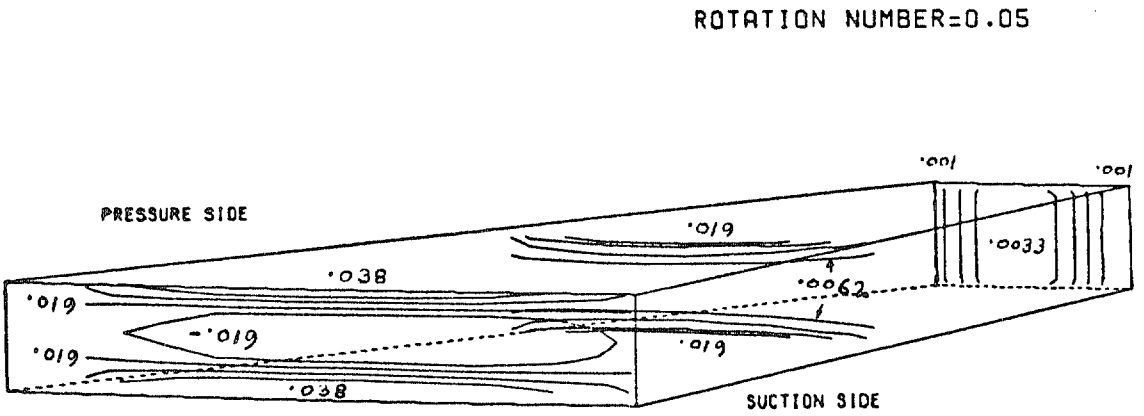

FIG. 8. A perspective view of the 'blade-to-blade' velocity [$\bar{u} = u/w_1$] contours at three different radial planes ($r/r_{tip} = 0{\cdot}33, 0{\cdot}66, 0{\cdot}97$); $Ro = 0{\cdot}05$, $R = 2 \times 10^5$, $N = 24$, $H_2/H_1 = 1$, $H_1/B_1 = 0{\cdot}5$.

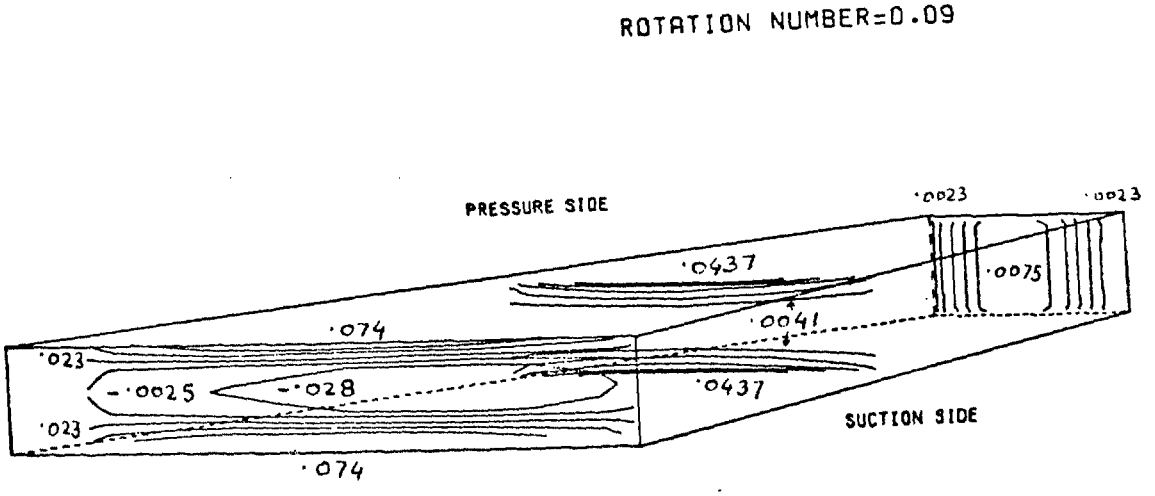

FIG. 9. A perspective view of the 'blade-to-blade' velocity $[\bar{u} = u/w_1]$ contours at three different radial planes $(r/r_{tip} = 0{\cdot}33, 0{\cdot}66, 0{\cdot}97)$; $Ro = 0{\cdot}09$, $R = 2 \times 10^5$, $N = 24$, $H_2/H_1 = 1$, $H_1/B_1 = 0{\cdot}5$.

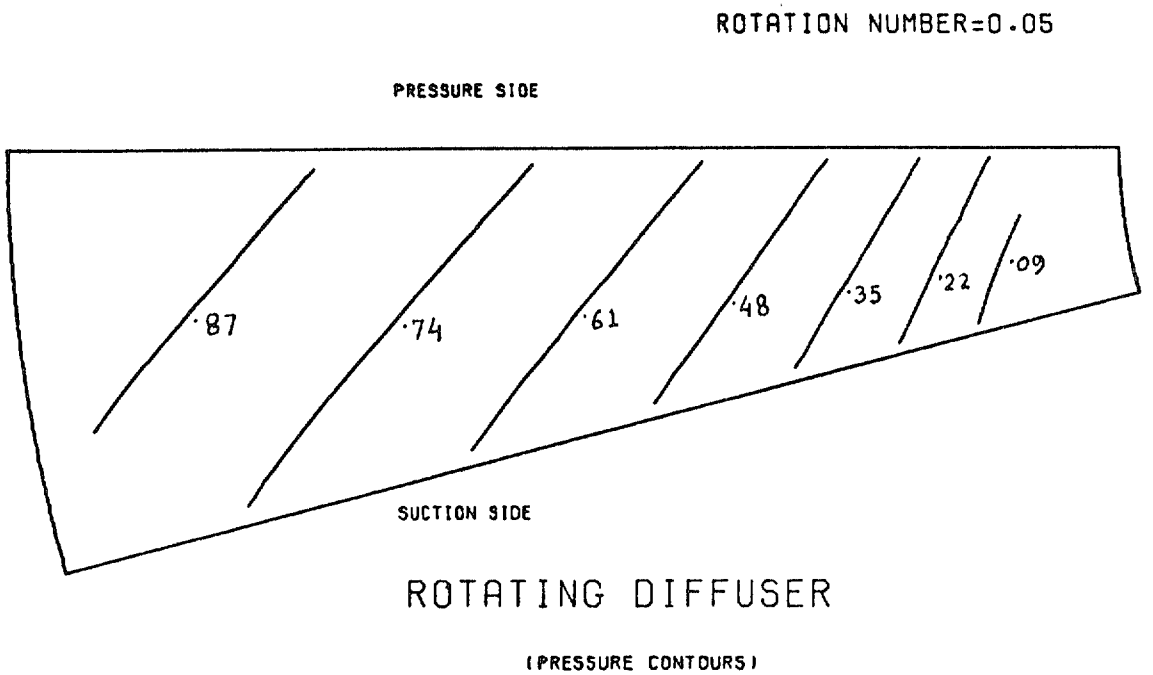

FIG. 10. Non-dimensional pressure ($\bar{p}$) distribution at the central plane ($Y/H = 0{\cdot}5$) of the diffuser;

$$\bar{p} = \frac{(p - \frac{1}{2}\rho\Omega^2 r^2) - (p_{\text{inlet,S}} - \frac{1}{2}\rho\Omega^2 r_{\text{inlet}}^2)}{\frac{1}{2}\rho\bar{w}_1^2}$$

$Ro = 0{\cdot}05$, $R = 2\times10^5$, $N = 24$, $H_2/H_1 = 1$, $H_1/B_1 = 0{\cdot}5$.

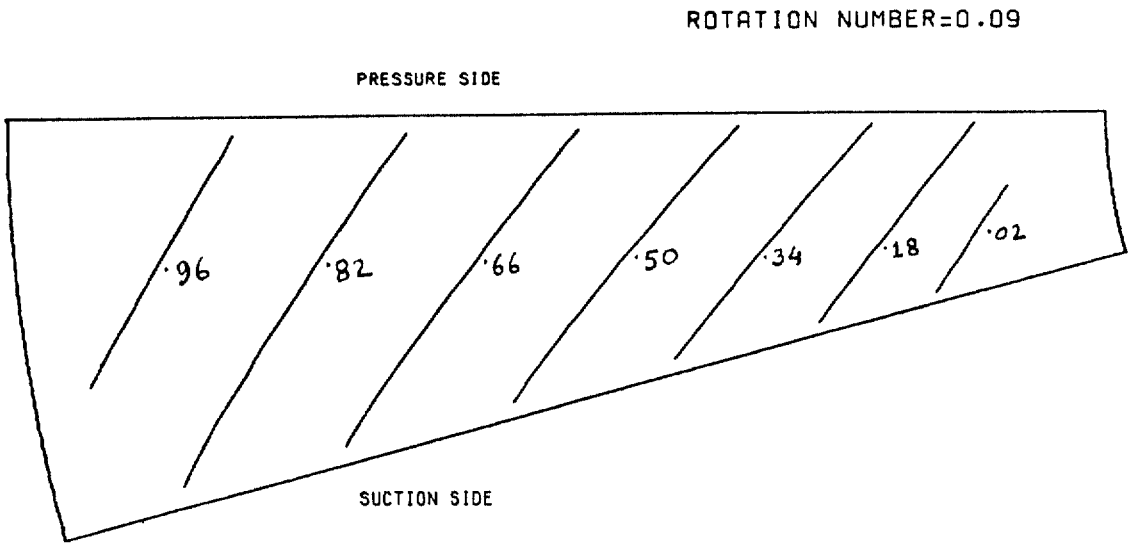

FIG. 11. Non-dimensional pressure distribution ($\bar{p}$) at the central plane ($Y/H = 0{\cdot}5$) of the diffuser;

$$\bar{p} = \frac{(p - \frac{1}{2}\rho\Omega^2 r^2) - (p_{\text{inlet,S}} - \frac{1}{2}\rho\Omega^2 r_{\text{inlet}}^2)}{\frac{1}{2}\rho\bar{w}_1^2}$$

$Ro = 0{\cdot}09$, $R = 2\times10^5$, $N = 24$, $H_2/H_1 = 1$, $H_1/B_1 = 0{\cdot}5$.

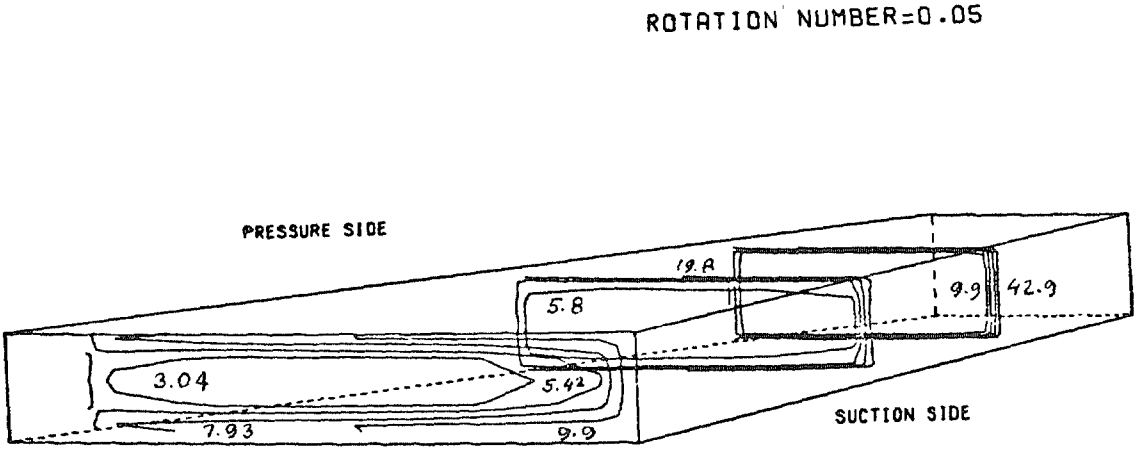

FIG. 12. A perspective view of turbulence energy $[\bar{k} = (k/\bar{w}_1^2) \times 10^4]$ contours at three different radial stations $(r/r_{tip} = 0{\cdot}5, 0{\cdot}66, 0{\cdot}97)$ $Ro = 0{\cdot}05$, $R = 2 \times 10^5$, $N = 24$, $H_2/H_1 = 1$, $H_1/B_1 = 0{\cdot}5$.

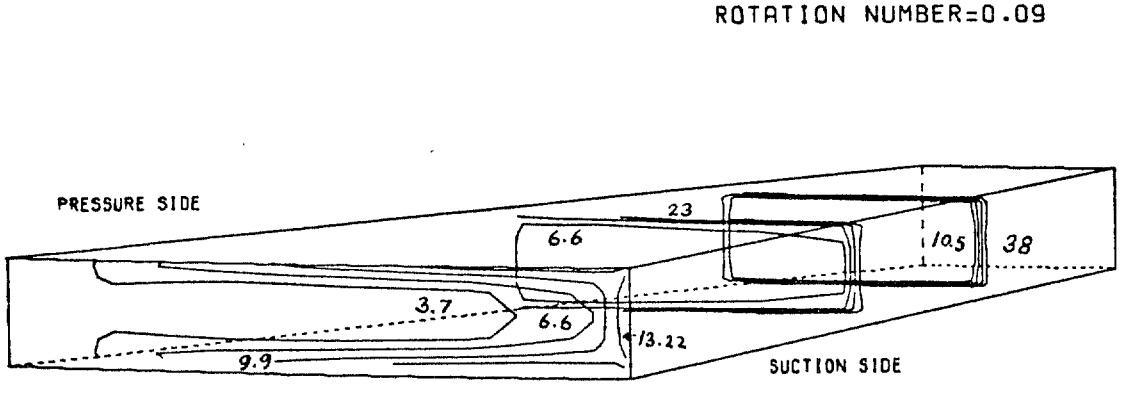

FIG. 13. A perspective view of turbulence energy $[\bar{k} = (k/\bar{w}_1^2) \times 10^4]$ contours at three different radial stations $(r/r_{tip} = 0{\cdot}5, 0{\cdot}66, 0{\cdot}97)$ $Ro = 0{\cdot}09$, $R = 2 \times 10^5$, $N = 24$, $H_2/H_1 = 1$, $H_1/B_1 = 0{\cdot}5$.

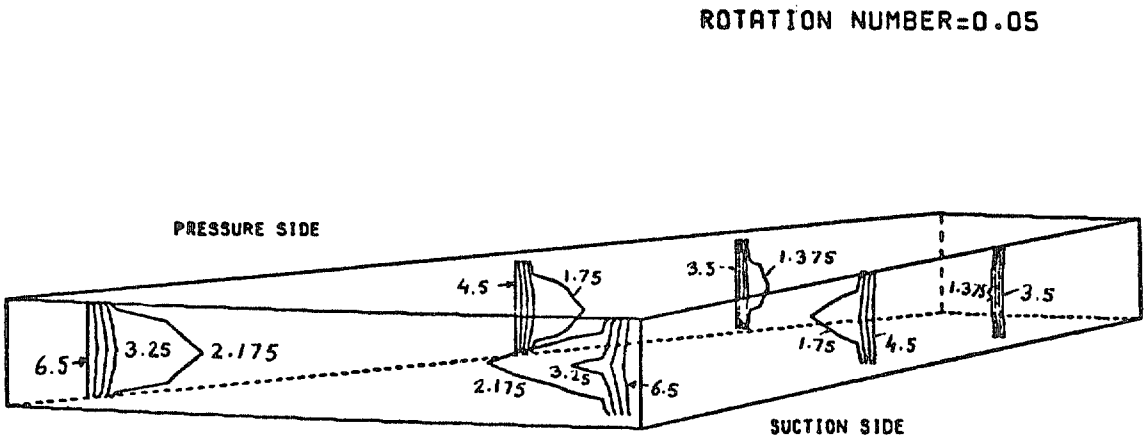

FIG. 14. A perspective view of turbulence length scale ($\bar{l} = l/H_1 \times 10^2$) contours at three different radial stations ($r/r_{tip} = 0{\cdot}5, 0{\cdot}66, 0{\cdot}97$); $Ro = 0{\cdot}05$, $R = 2 \times 10^5$, $N = 24$, $H_2/H_1 = 1$, $H_1/B_1 = 0{\cdot}5$.

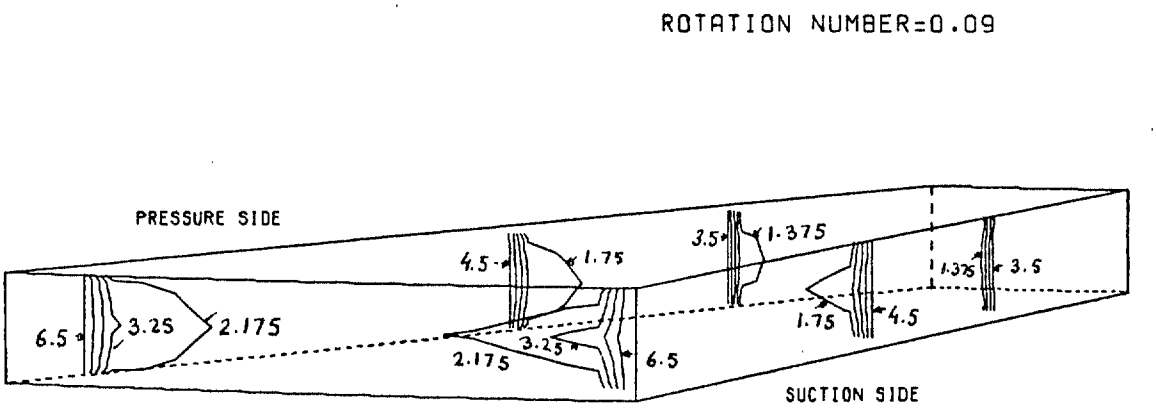

FIG. 15. A perspective view of turbulence length scale ($l = l/H_1 + 10^2$) contours at three different radial stations ($r/r_{tip} = 0{\cdot}5, 0{\cdot}66, 0{\cdot}97$); $Ro = 0{\cdot}09$, $R = 2 \times 10^5$, $N = 24$, $H_2/H_1 = 1$, $H_1/B_1 = 0{\cdot}5$.

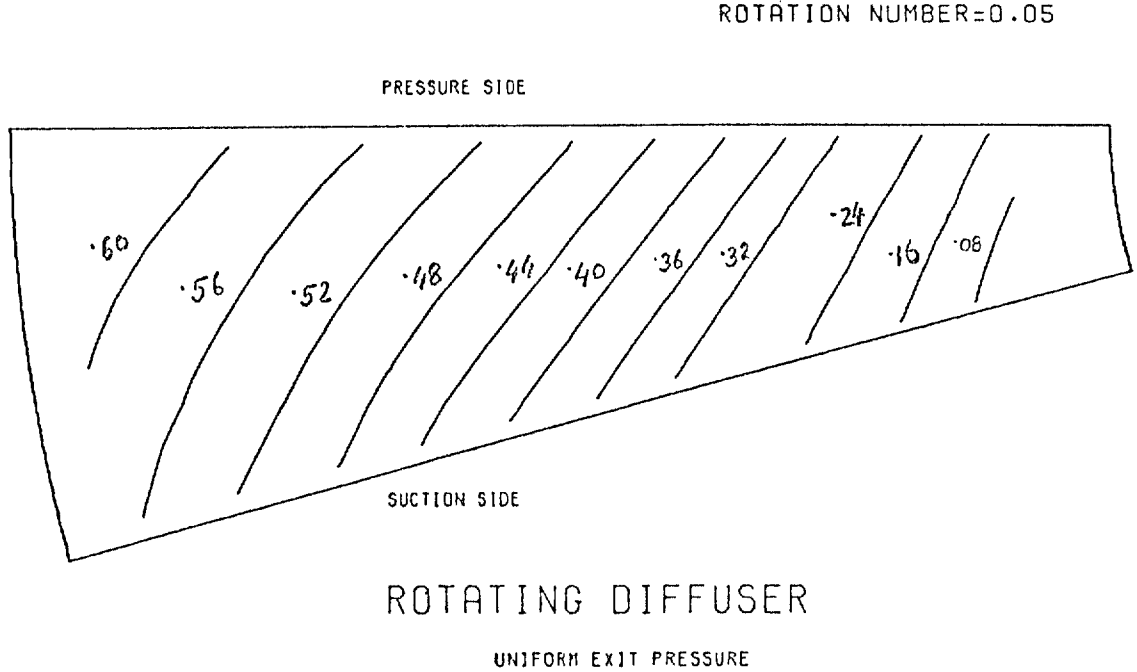

FIG. 16. Non-dimensional pressure distribution ($\bar{p}$) at the central plane ($Y/H = 0{\cdot}5$) of the diffuser; uniform exit pressure distributions is assumed.

$$\bar{p} = \frac{(p - \frac{1}{2}\rho\Omega^2 r^2) - (p_{\text{inlet,S}} - \frac{1}{2}\rho\Omega^2 r_{\text{inlet}}^2)}{\frac{1}{2}\rho\bar{w}_1^2}$$

$Ro = 0{\cdot}05$, $R = 2 \times 10^5$, $N = 24$, $H_2/H_1 = 1$, $H_1/B_1 = 0{\cdot}5$.

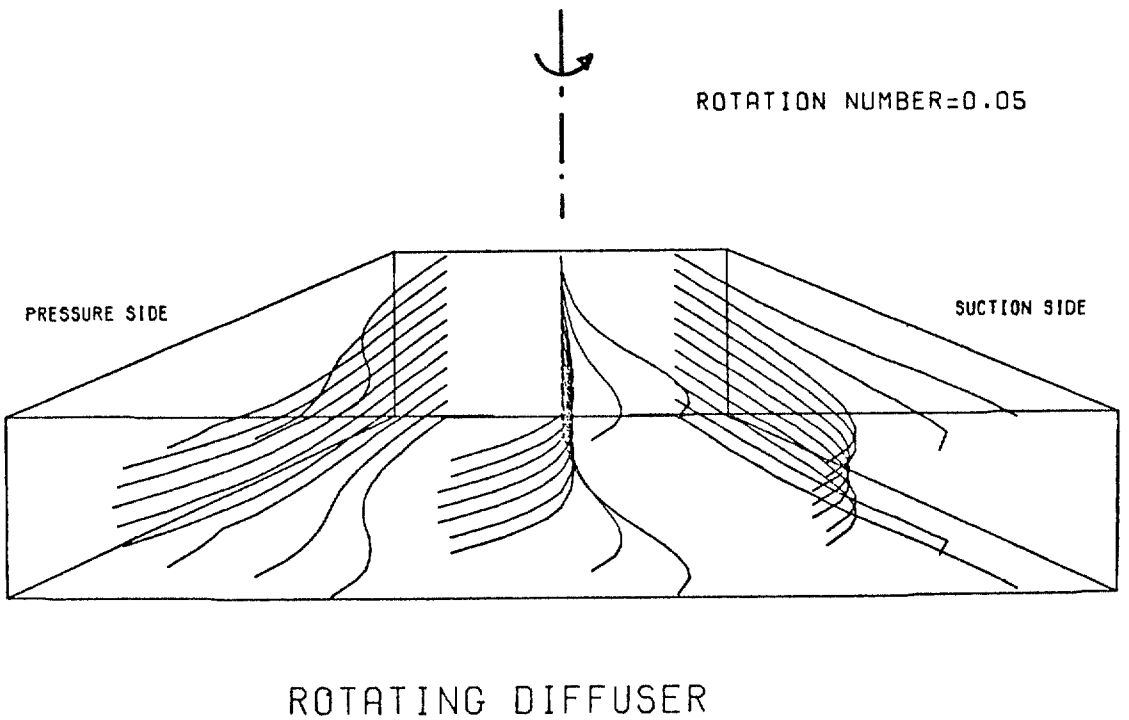

FIG. 17. A perspective view of particle tracks in rotating diffuser with uniform exit pressure distribution $Ro = 0{\cdot}05$, $R = 2 \times 10^5$, $N = 24$, $H_2/H_1 = 1$, $H_1/B_1 = 0{\cdot}5$.

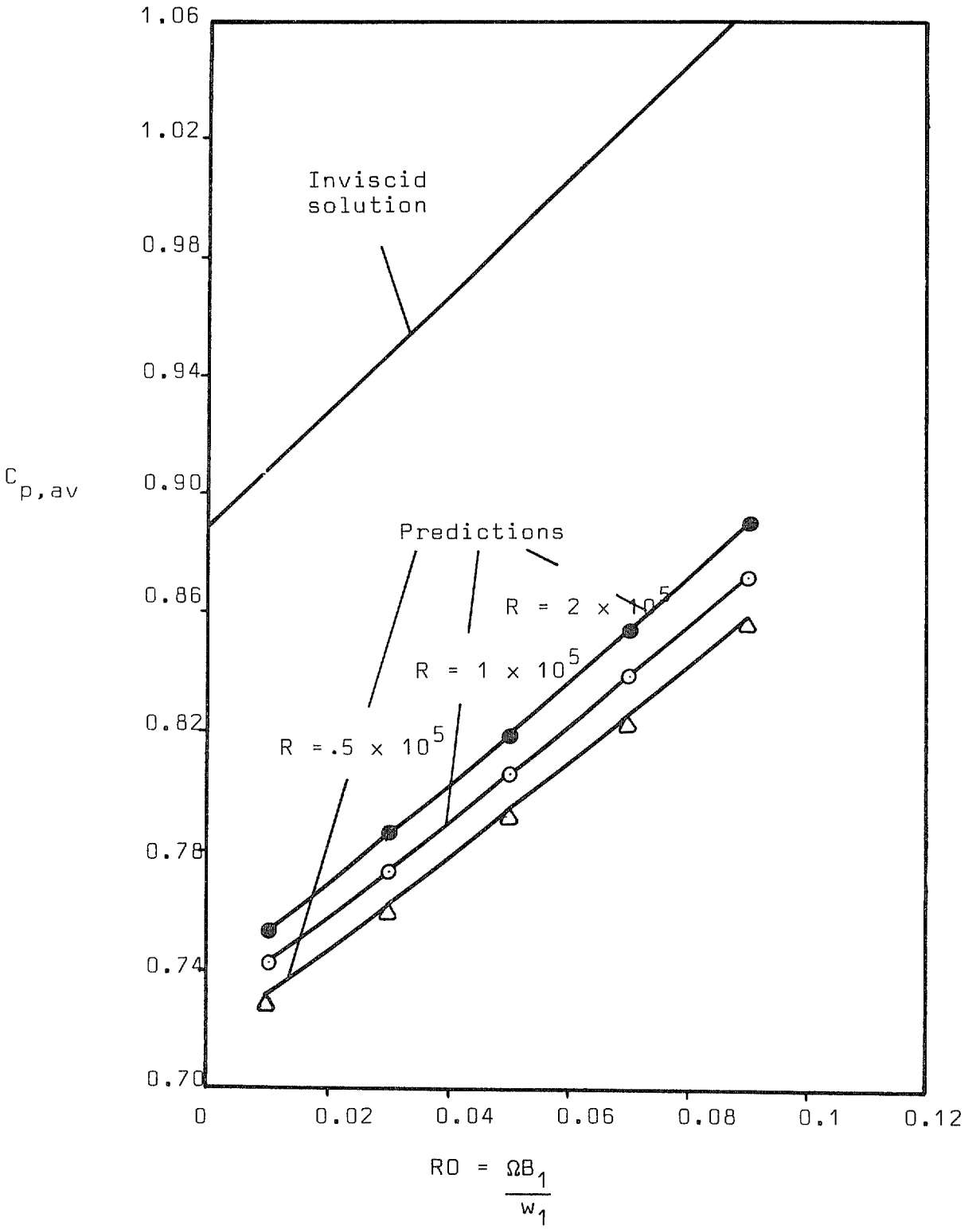

FIG. 18. Predicted effect of Reynolds number on pressure rise characteristics;

$$C_{P,\mathrm{av}} = \tfrac{1}{2}|C_{P,\mathrm{P}} + C_{P,\mathrm{S}}|$$

$$C_P = \frac{(p_{exit} - \frac{1}{2}\rho\Omega^2 r_{\mathrm{tip}}^2) - (p_{inlet,S} - \frac{1}{2}\rho\Omega^2 r_{\mathrm{inlet}}^2)}{\frac{1}{2}\rho\bar{w}_1^2}$$

$r_{\mathrm{tip}}/r_{\mathrm{inlet}} = 3{\cdot}0$, $N = 24$, $H_1/B_1 = 0{\cdot}5$, $H_2/H_1 = 1{\cdot}0$.

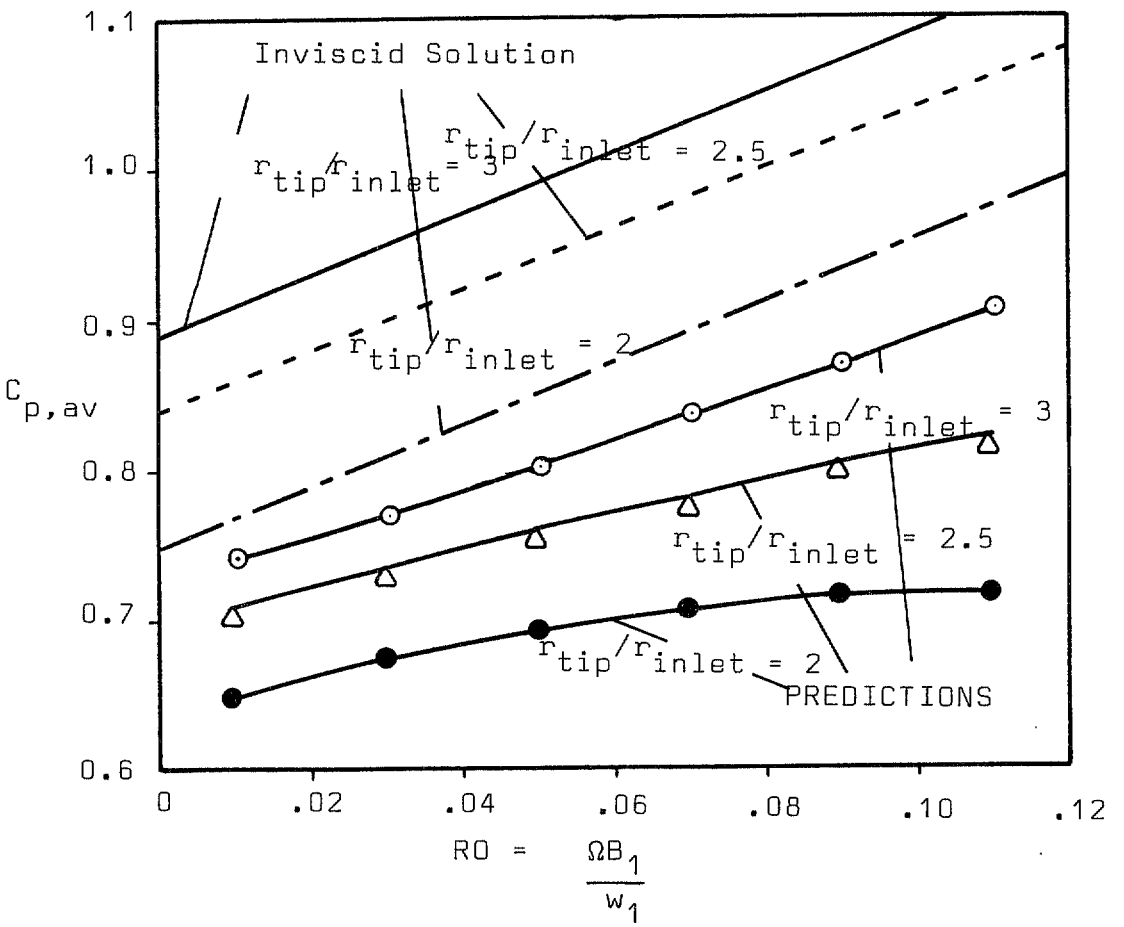

FIG. 19. Predicted effect of radius ratio on pressure rise characteristics; $N = 24$, $R = 1 \times 10^5$, $H_1/B_1 = 0{\cdot}5$, $H_2/H_1 = 1{\cdot}0$.

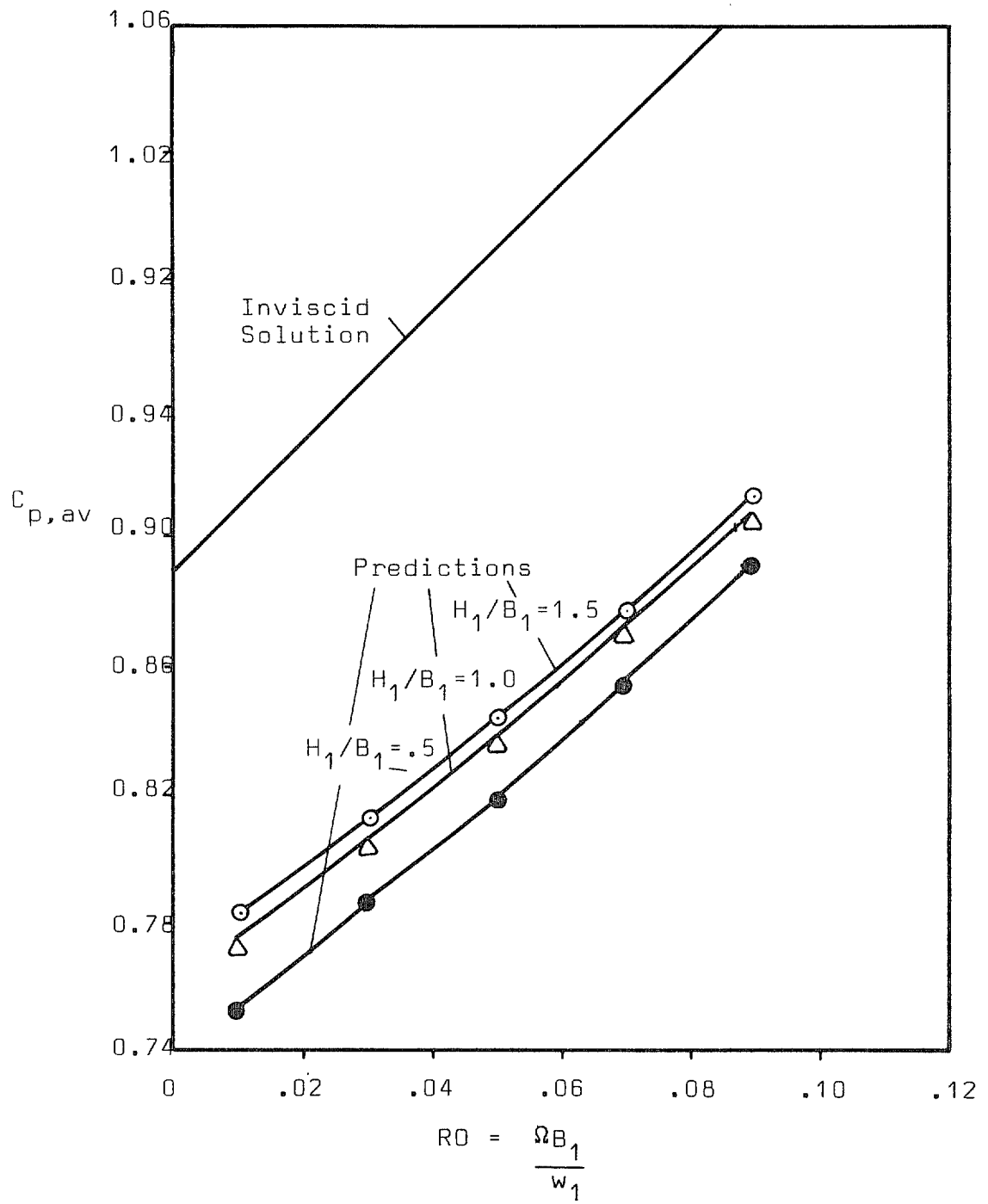

FIG. 20. Predicted effect of inlet aspect ratio on pressure rise characteristics; $R = 2 \times 10^5$, $r_{tip}/r_{inlet} = 3{\cdot}0$, $N = 24$, $H_2/H_1 = 1$.

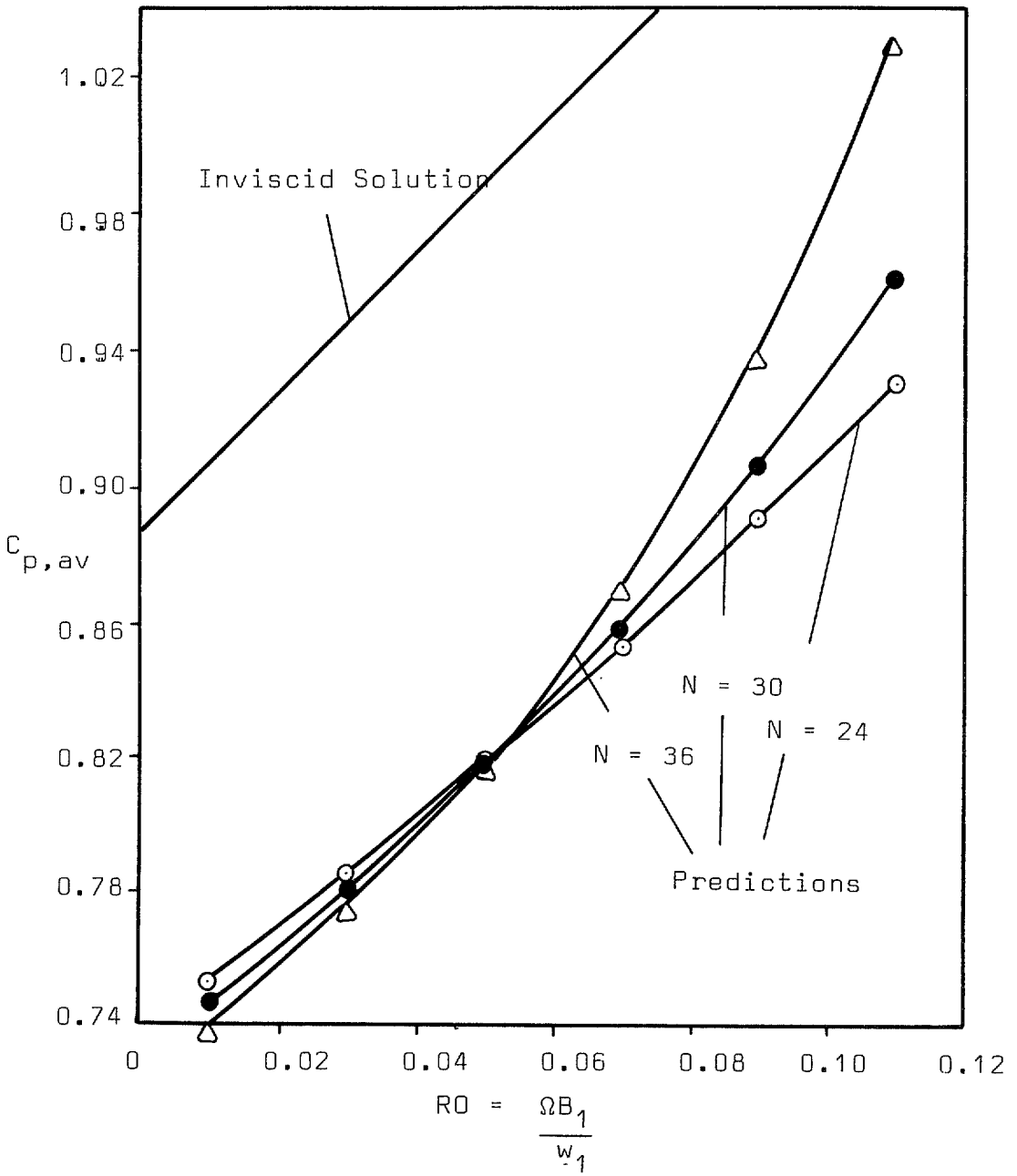

FIG. 21. Predicted effect of number of blades on pressure rise characteristics; $r_{tip}/r_{in} = 3{\cdot}0$, $H_1/B_1 = 0{\cdot}5$, $H_2/H_1 = 1$, $N = 30$, $R = 2 \times 10^5$.

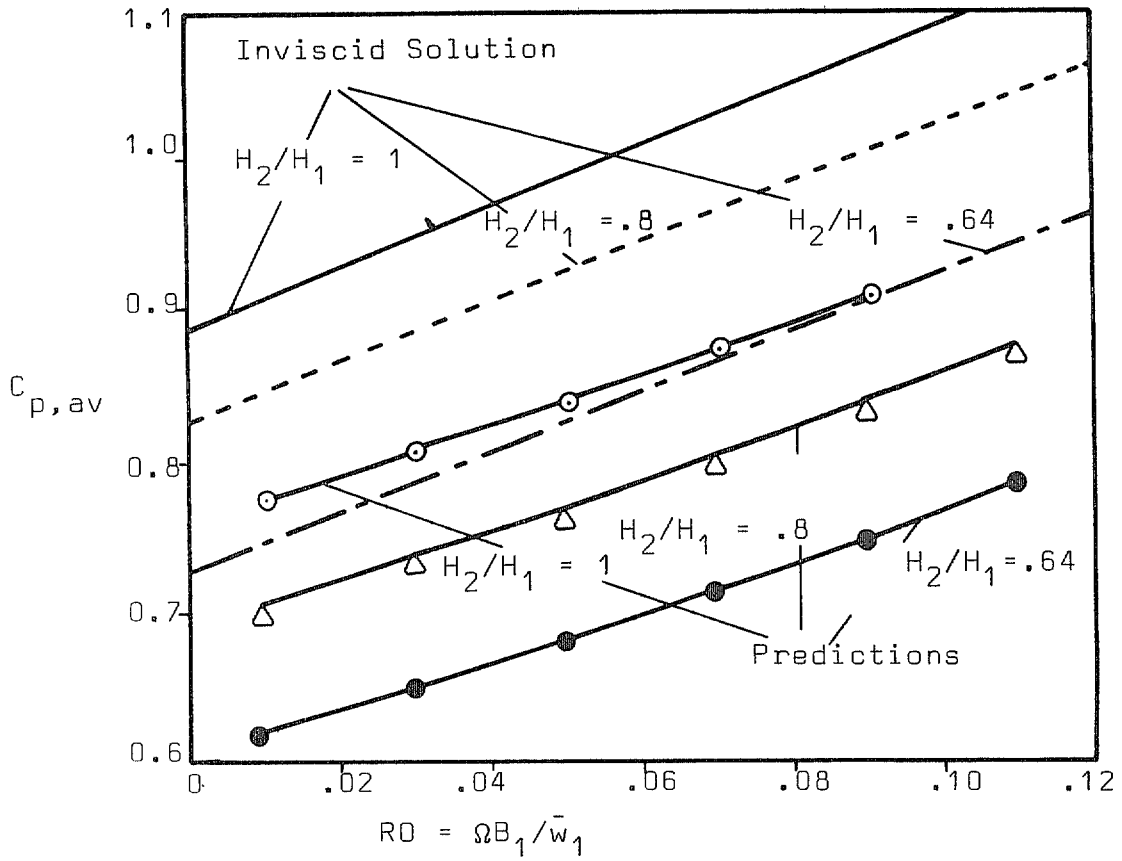

FIG. 22. Predicted effect of exit to inlet height ratio on pressure rise characteristics; $r_{tip}/r_{inlet} = 3{\cdot}0$, $H_1/B_1 = 1{\cdot}0$, $N = 24$, $R = 2 \times 10^5$.

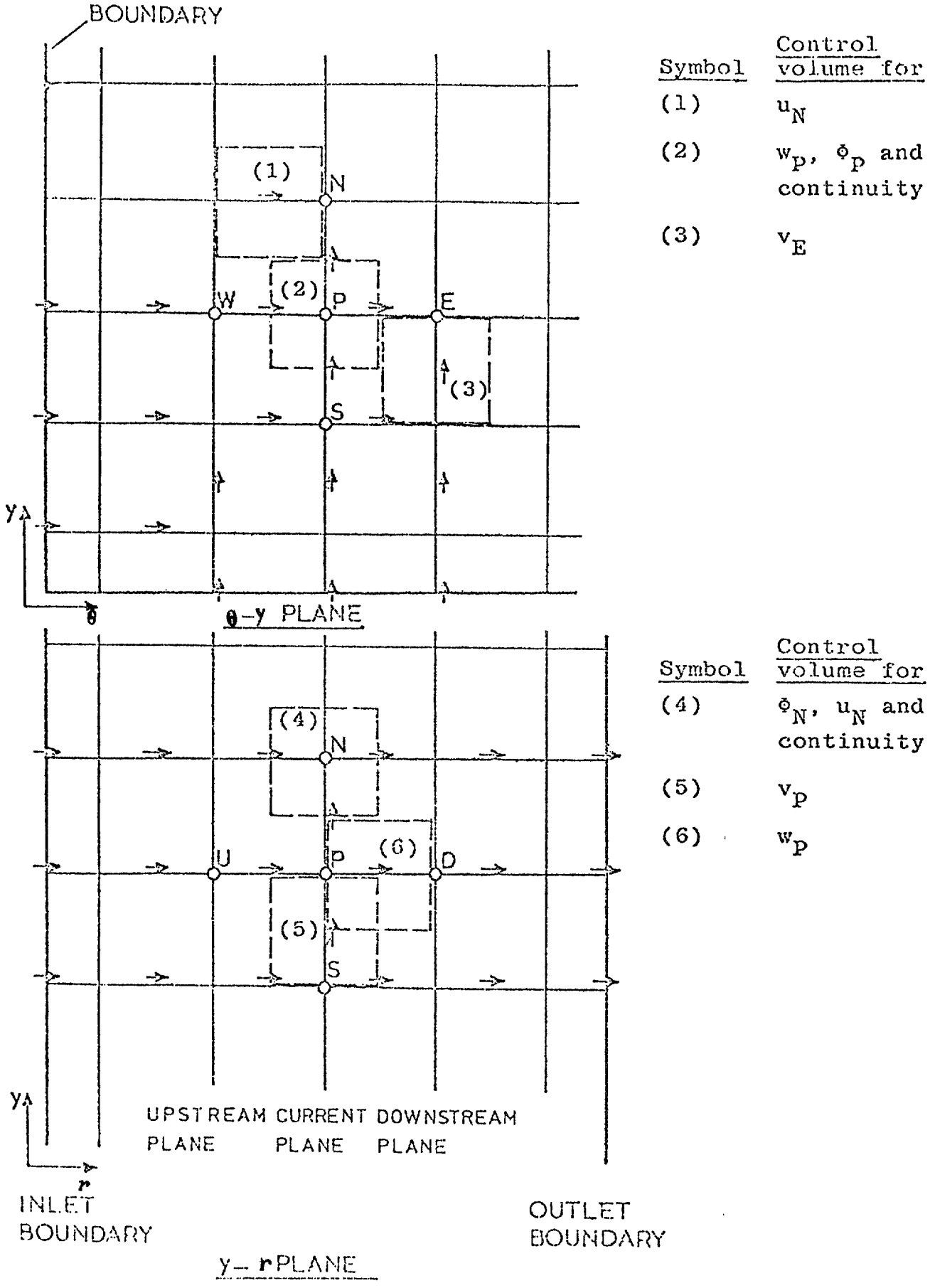

FIG. 23. Definition of control volumes.

Printed in England for Her Majesty's Stationery Office by J. W. Arrowsmith Ltd., Bristol BS3 2NT
Dd. 587484 K.5. 1/78

HER MAJESTY'S STATIONERY OFFICE

Government Bookshops

49 High Holborn, London WC1V 6HB
13a Castle Street, Edinburgh EH2 3AR
41 The Hayes, Cardiff CF1 1JW
Brazennose Street, Manchester M60 8AS
Southey House, Wine Street, Bristol BS1 2BQ
258 Broad Street, Birmingham B1 2HE
80 Chichester Street, Belfast BT1 4JY

Government Publications are also available through booksellers

ISBN 0 11 471143 7